JOURNAL OF Materials CHEMISTRY
Feature Article

Structure and reactivity of oxide surfaces: new perspectives from scanning tunnelling microscopy

Russell G. Egdell and Frances H. Jones
Inorganic Chemistry Laboratory, South Parks Road, Oxford, UK OX1 3QR

Scanning tunnelling microscopy (STM) has emerged in the past few years as a uniquely powerful tool for the investigation of oxide surfaces. STM is capable of real-space imaging of periodic structures with atomic resolution and of characterising local atomic arrangements associated with defect sites. The power of the technique is further enhanced by the ability to probe filled and empty density of states profiles at specific atomic sites by monitoring variations in tunnelling currents with applied voltage. The interpretation of STM images is not always unambiguous, a question of central importance being whether oxygen or metal ions appear as maxima in the images. The necessity for adequate sample conductivity imposes some constraints on the applicability of the technique, although developments in instrumentation and in techniques for sample preparation are helping to overcome these limitations. The range and limitations of the technique are illustrated by reference to work on tungsten oxides, titanium dioxide and iron oxides. The review concludes with a discussion of recent developments in the study of molecular adsorbates.

1 Introduction

There has been a huge upsurge in interest over the past few years in the surface properties of metal oxides. This has been driven in part by the technological importance of these materials in areas such as catalysis and gas sensing, where surface properties are of crucial importance, and in part by a continuing fascination with the diverse range of structural, chemical and electronic properties exhibited by oxides. One major aim of academic surface science is to characterise surface structure at an atomic level and to develop an understanding of the ways in which molecules interact with specific surface sites. Most technological applications involve polycrystalline material, but the starting point for tackling the objectives outlined above usually lies in the study of well defined single crystal surfaces under ultrahigh vacuum (UHV) conditions.[1,2] The intrinsic complexity of oxides is reflected in the fact that even now only a handful of these idealised surface structures have been solved by diffraction techniques using electrons or X-rays. Moreover, there is a general consensus that the chemical reactivity of oxide surfaces is probably dominated in many cases by defects. Diffraction techniques offer the prospect of rigorous determination of periodic surface structures, but are unsuited to investigation of local structure associated with defect sites. Scanning tunnelling microscopy (STM) allows imaging of both periodic and defect structures with atomic resolution. Moreover, by measuring the variation of tunnelling current with applied voltage it is possible to obtain a measurement of filled and empty densities of states. STM therefore seems to be the ideal tool for tackling many of the outstanding problems in oxide surface science.

STM made its debut in 1982 by providing a real space solution to the surface structure of Si(111) (7×7). Extension of the technique to other semiconductor surfaces and to metal surfaces followed in rapid succession and by about 1990 it had become a routine matter to obtain high quality images on surfaces of this type. Related techniques using the technology of STM also appeared, notably atomic force microscopy (AFM). In the 1990s the field has settled into a period of maturity with established series of national and international conferences devoted to scanning probe microscopy and with the appearance of several textbooks.[3,4]

Against this background, the application of STM to oxide surfaces developed very slowly in the initial years. Henrich and Cox's definitive monograph on oxide surface science[1] published in 1994 presented only two images where anything approaching atomic resolution had been achieved on an oxide surface and concluded that although 'the results are encouraging they have not yet been of real value in a surface structure determination on oxides.' An exception to this statement was the acquisition before 1990 of atomically resolved images from cleavage surfaces of layered oxide superconductors, particularly $Bi_2Sr_2CaCu_2O_8$[5–7] and $Tl_2Ba_2CaCu_2O_8$.[8] However as will be seen below these are very 'easy' surfaces to work with because of the weak interlayer bonding and the inertness of cleavage surfaces. The application of STM to oxide superconductors has already been reviewed[9] and in the present contribution we focus attention on materials other than the cuprates. Within the past four years many of the apparent difficulties in studying these surfaces have been overcome and there is now a rapidly growing body of work where STM has provided definitive information about surface structure.

The organisation of this review paper is as follows. We first present a general introduction to the technique of STM. Next we address the important question of interpretation of STM images, touching on the interplay between structural and electronic effects which is of particular importance when dealing with oxides. Experimental problems associated with sample conductivity are then assessed, followed by a discussion of the merits of carrying out STM measurements in UHV rather than under ambient conditions. The ideas introduced in the earlier sections are illustrated by reference to work on the tungsten oxides WO_3[10–14] and Na_xWO_3,[15–17] on the rutile form of TiO_2,[18–36] and on the iron oxides Fe_2O_3[37,38] and Fe_3O_4.[39–44] Finally some recent developments in the study of adsorbates on oxide surfaces are highlighted.[45–47] Here there are clear indications that STM is not only a tool for investigation of static surface structures, but that it is also able to give a real time view of dynamic processes, such as molecular decomposition and diffusion.

2 The technique of STM

2.1 Background

STM relies on quantum mechanical tunnelling. An atomically sharp tip is brought within a few Ångstroms of a surface using an arrangement of piezoelectric transducers and a voltage is applied between the tip and the sample: here we adopt the usual convention of quoting the bias of the sample relative to

the tip. At small separations the wavefunctions for electron states at the surface overlap with the wavefunctions associated with the tip and electrons may tunnel into or out of the surface, depending on the bias. The tunnelling current shows an exponential variation with tip–surface separation because of the exponential decay of the wavefunctions into the vacuum. The tip is moved parallel to the surface in the xy plane whilst the z position (*i.e.* the distance from the surface) is controlled. In most cases the xy scanning involves a sawtooth variation in x with progressive increments in y. There are two principal modes of image acquisition. In the constant height mode the tunnel current is simply measured as a function of xy coordinates. In the alternative constant current mode a negative feedback is applied to the z piezo to keep the tunnel current constant and the z displacement is monitored as a function of xy coordinates. The constant height mode allows for more rapid scanning across the surface but there is a significantly larger risk of 'tip crash' on surfaces containing irregular protrusions or large numbers of steps. Constant current imaging is therefore more usual. The image is built up from a series of corrugation profiles, *i.e.* plots of z displacement as a function of x displacement. These are finally transformed into greyscale images which represent maximum outward z displacement as white and maximum inward displacement as black. These images may in turn be enhanced by various filtering techniques, application of alternative colour schemes and by transformation into 'false' 3D views which usually overemphasise the z corrugation. Most commercial software allows the bias voltage to be changed between the forward x sweep and the reverse, so that two images of exactly the same area of the sample can be acquired synchronously at different bias. In addition the feedback loop may be disengaged at each pixel point in the image and a current–voltage (I–V) curve measured at that point. It may be shown that the normalised differential conductance $(\mathrm{d}I/\mathrm{d}V)/(I/V)$ is directly proportional to the filled or empty density of states. Thus STM complements photoemission spectroscopy (PES) and inverse photoemission spectroscopy (IPES) in providing atomically resolved electronic structure information. However, the spatial characterisation of electronic states is gained at the expense of information about the crystal momentum, which is provided by the E–k dispersion curves derived from PES and IPES.

2.2 General considerations in the interpretation of STM images of oxides

A typical STM image of an oxide surface will contain an ordered array of greyscale maxima and minima, usually interspersed with steps, dislocations and other defects. It is rarely the case that all ions within the surface unit cell show up as greyscale maxima. A major issue of interpretation is therefore to establish the correspondence between maxima in greyscale images and atomic positions within the unit cell. In general oxygen anions and metal cations may have the same surface periodicity, so the corrugation profiles do not in themselves solve this problem in all cases and there is therefore scope for controversy! The problems of interpretation are illustrated by some experiments we have carried out[48] on a (4×1) reconstruction on $SnO_2(110)$ (Fig. 1). Here features which appear as depressions in the $+1.5$ V image transform into bright maxima in the image taken at lower sample bias. This implies that the images cannot be explained solely in terms of topography and consideration of electronic structure is crucial. An additional complication is that image contrast may depend on the state of the tip. In the case of the simple adsorbate system of O on Cu(110) the image contrast may be totally reversed by the deliberate adsorption of an oxygen atom onto the tip.[49] Thus at $+0.03$ V sample bias and 1 nA tunnel current oxygen adatoms appear as 'Mexican hat' maxima when imaged with a tip that has been rigorously cleaned by field emission, but when the tip is deliberately dipped into an oxygen-rich area of the surface (allowing transfer of O atoms onto the tip), the adatoms are imaged as minima (Fig. 2).

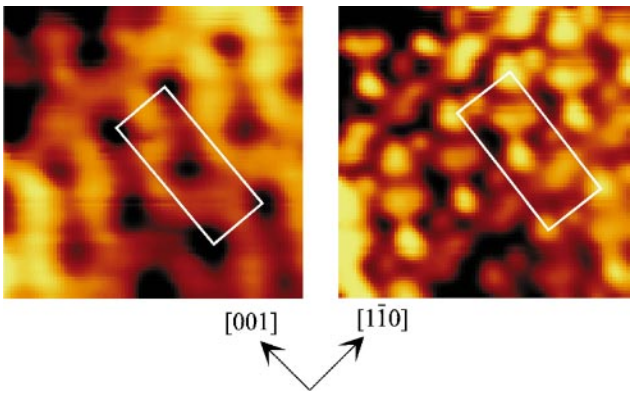

Fig. 1 Two sequentially acquired 25 Å × 25 Å images from the (4×1) reconstructed surface of $SnO_2(110)$, both with 1 nA tunnel current. The left hand image is taken at $+1.5$ V sample bias, the right hand at $+1.0$ V bias. The same unit cell is highlighted in each image. Note the reversal of topographic contrast. A third image taken at $+1.5$ V bias was very similar to the first, indicating that there had been no tip change. Adapted from ref. 48.

2.3 Models of STM

Most qualitative interpretations of STM images are based implicitly on the Tersoff–Hamann model.[50] Here the tip electronic wavefunctions are assumed to be described by spherically symmetrical s-waves. For small sample bias it may be shown that the tunnelling current I is given by:

$$I \propto \sum_{\mathrm{s}} |\Psi_{\mathrm{s}}(\boldsymbol{r}_0)|^2 \delta(E_{\mathrm{s}} - E_{\mathrm{f}}) \qquad (1)$$

where the summation is taken over amplitudes of sample wavefunctions s at the centre of the tip whose coordinates are specified by $\boldsymbol{r}_0$ and the subscripts refer to the energy of electronic states in the sample (s) relative to the Fermi energy of the tip (f). By definition the summation corresponds to the local density of sample electronic states at the centre of curvature of the tip and therefore the constant current images correspond to contours of constant density of sample electronic states. Taking explicit account of the decay of the sample and tip wavefunctions into the tunnelling gap we have:

$$I \propto \sum_{\mathrm{s}} |\Psi_{\mathrm{s}}|^2 \exp -[2\kappa(R+s)]\delta(E_{\mathrm{s}} - E_{\mathrm{f}}) \qquad (2)$$

where R is the tip radius and s is the tip to sample separation. The decay constant κ is given by:

$$\kappa = \sqrt{(8\pi^2 m\phi/h^2)} \qquad (3)$$

where m is the electron mass and ϕ is the local surface barrier. If s is in Ångstroms and ϕ is in eV, κ can be expressed in a simple numerical form:

$$2\kappa = 1.025\sqrt{\phi} \qquad (4)$$

For very large sample–tip separations, the surface barrier would be expected to be simply the average of sample and tip workfunctions. However, at the separations appropriate to most STM experiments, the slow decay of exchange correlation potentials causes ϕ to be much less than the workfunction. In fact ϕ can be determined experimentally from the relationship:

$$\phi = 0.952(\mathrm{d}\ \ln I/\mathrm{d}s)^2 \qquad (5)$$

One reported value of 1.6 eV for the oxide surfaces $Na_{0.82}WO_3(001)$[15] is much less than typical oxide workfunctions of the order 4–5 eV.

There are already many approximations at this stage. Most

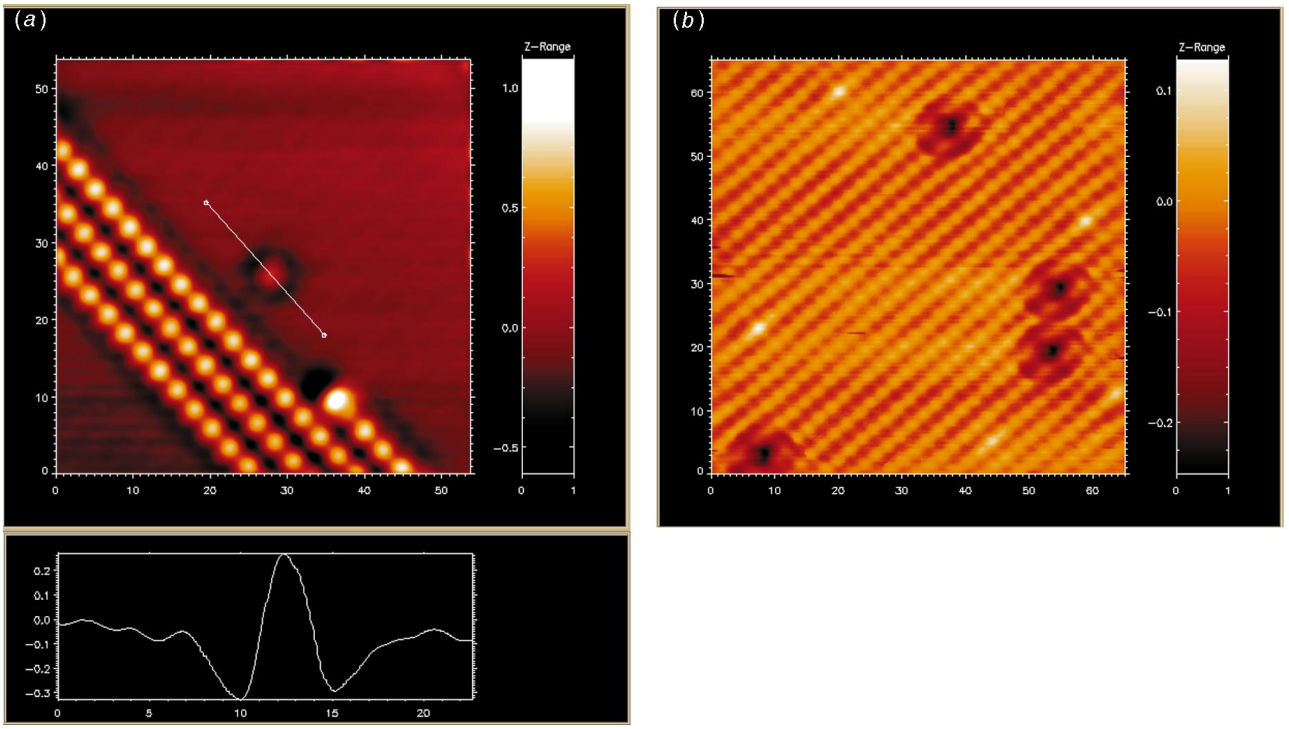

Fig. 2 (*a*) 50 Å × 50 Å STM image of Cu(110) exposed to oxygen and then cooled to 4 K. Image taken with a cleaned Pt/Ir tip at 0.03 V sample bias and 1 nA tunnel current. Rows of the O induced (2 × 1) reconstruction are apparent, along with an isolated O atom that appears as a 'Mexican hat' in the corrugation profile shown under the image in the central panel. (*b*) 65 Å × 65 Å image now taken with an O terminated tip. The four isolated O atoms now appear as greyscale minima. Reproduced with permission from ref. 49.

notably, STM experiments almost invariably use W or Pt/Ir tips and if these do indeed terminate with a single transition metal atom, the tip wavefunctions will certainly not be a s wave. For example, model calculations on a cluster providing a realistic model of a W tip revealed a strong $5d_{z^2}$ resonance near the Fermi level.[51] In general predominance of directional tip states of this sort will lead to greatly enhanced surface corrugation.

Notwithstanding these difficulties eqn. (2) can be cast into a very simple form[15] that allows rudimentary qualitative interpretation of STM images from compound materials such as oxides:

$$I(x,y,z) \propto \sum_i D_i \exp -(1.025 s_i \sqrt{\phi}) \qquad (6)$$

Here the current I for a tip at position (x,y,z) is a summation over contributions from atoms i on the surface in the proximity of the tip. The atoms are assumed to be hard spheres separated from the surface of the hard sphere tip by distances s_i and the parameter D_i gives a measure of the relative contribution of each atom to the total density of electronic states at the energy appropriate to the tunnelling conditions which are being used. Eqn. (6) tells us that when performing constant current imaging of a flat surface containing atoms of two types, say j and k, a density of states ratio $D_j/D_k = 0.1$ will translate into an apparent topographic height difference between the two atoms such that $s_j - s_k = 1.77$ Å. The highly ionic nature of oxides means that density of states ratios of this order are not fanciful and electronic structure effects will exert a major influence on topographic images.

A more direct approach to dealing with electronic structure effects is to evaluate the square of sample wavefunctions above the surface [the ψ_s^2 of eqn. (2)] in an explicit fashion. This approach has been developed by Gulseren *et al.*[31] using a first-principles atomic-orbital based scheme that was benchmarked against more rigorous *ab initio* plane wave pseudo-potential calculations. In particular they calculated charge densities in conduction band states up to 1.5 eV above the Fermi level at various heights above a $TiO_2(110)$ surface in an attempt to understand experimental empty state images from that surface. In a similar spirit, Diebold *et al.*[30] computed contour plots of empty state charge density for $TiO_2(110)$ using a full plane wave pseudo-potential method implemented within the local density approximation. These calculations are discussed in Section 3. A limitation in this approach is that no explicit account can be taken of the influence of tip structure on STM images.

A potentially important recent development in interpretation of STM images of oxides has been direct calculation of tunnelling currents using the so-called electron scattering quantum chemistry (ESQC) approach. Here the tip, surface and gap are treated as an impurity in an otherwise perfect conductor and both the tip and surface can act as sources and sinks of electrons. The tip is modelled explicitly as a well defined cluster and impurity atoms may be added to the tip at will. This model has been used with notable success to treat adsorbed C_6H_6 molecules on Rh(111)[52] and ordered layers of S on Re(0001).[53] In the latter system adsorption of a single S atom onto a single Pt (1-Pt) or 3-Pt terminated tip led to contrast reversal for S atoms adsorbed at on-top positions. The model has recently been extended to treat an FeO(111) layer on Pt(111).[54] Here it is found that topographic maxima in the images occur over O positions for Pt terminated tips but over Fe positions for O terminated tips.

3 Experimental aspects of STM

3.1 Sample conductivity: which oxides can be studied and which cannot?

The tunnel current flowing in an STM is typically of the order 0.1–20 nA. There is an obvious requirement that the sample should have sufficient conductivity to allow passage of the tunnel current. Experience with a number of oxides indicates that a conductivity of the order of 1 Ω^{-1} cm^{-1} is necessary to allow trouble free imaging.

The conductivity requirement is obviously satisfied by metallic oxides. Those that have been imaged with atomic resolution include a number of high temperature oxide superconductors such as $Bi_2Sr_2CaCu_2O_{8-x}$ and its substituted derivatives,[5–7,55–61] $Tl_2Ba_2Ca_{1+n}Cu_{2+n}O_{8+2n}$,[8,62,63] $Pb_2Sr_2(Y,Ca)Cu_3O_8$[64] and $YBa_2Cu_3O_7$,[65–69] ReO_3,[70] WO_2[71] and sodium tungsten bronzes[15–17] Na_xWO_3 together with oxide bronzes such as the blue bronzes $M_{0.3}MoO_3$,[72–77] and Fe_3O_4 whose room temperature conductivity is very high if not truly metallic.[39–43] For materials which are metallic, filled electronic states below the Fermi level can be accessed at positive sample bias and empty states at negative sample bias, so that STM imaging should be possible at either positive or negative sample bias.

At the other extreme, low conductivity rules out the study of important wide bandgap main group oxides such as MgO and Al_2O_3, although even materials of this sort can be studied at very low resolution if decorated with a thin conducting layer of a metal such as Au.[78] So far as we are aware there have been no studies to date on bulk oxide crystals whose conductivity is dominated by ion transport and which have low electronic conductivity (*e.g.* Y or Ca doped ZrO_2).

Maximal oxidation state transition metal oxides with a d^0 configuration typically have bandgaps in excess of 2 eV and are intrinsically poor conductors if truly stoichiometric. However, annealing in UHV or a partial pressure of hydrogen induces bulk oxygen loss. The resulting d^1 donor levels usually sit close to the conduction band minimum so that these materials become extrinsic n-type semiconductors. UHV annealed TiO_2,[18–36] WO_3,[10–14] $SrTiO_3$[79–82] and $BaTiO_3$[83] all acquire sufficient conductivity to be studied by UHV STM. The number of filled donor states is usually small in relation to the number of empty conduction band states. Thus it is possible to image these surface by tunnelling into empty states at negative sample bias, but filled state imaging is more difficult unless the bias is sufficient to access filled O 2p levels. An alternative approach to increasing conductivity that has been used with V_2O_5 is to dope with a very small concentration of an interstitial alkali metal during crystal growth,[84,85] although it should be noted that even the undoped material will sustain tunnelling in air.[86] Likewise the intergrowth bronze $Rb_{0.03}WO_3$ has been imaged.[87] Finally for sufficiently high levels of reduction the oxygen vacancies in d^0 transition metal oxides will arrange themselves into ordered crystallographic shear planes giving rise to distinct new Magnèli-type phases. These may be metallic or have very low activation energies for conduction and most will probably be amenable to STM investigation. In some recent elegant experimental work Rohrer and coworkers have followed the evolution of surface structure in the series MoO_3, $Mo_{18}O_{52}$, Mo_8O_{23}, Mo_4O_{11}, although the parent insulating MoO_3 was studied by AFM rather than STM.[88,89]

Binary or ternary d^n oxides of the later first row transition elements are usually Mott–Hubbard or charge transfer insulators with a localised d^n configuration. Comparatively few of these materials (again excluding the special case of oxide superconductors and their parent phases) have been studied by STM, one notable exception being Fe_2O_3 which under UHV has a propensity to lose oxygen to give Fe_3O_4 or even FeO-like surfaces.[37,38] In a chemical sense the conductivity is again n-type. Marginally conducting p-type oxides pose a greater technical challenge. Mobile holes are introduced by oxidation of the system by introduction of interstitial oxygen or cation vacancies, or by substitution of a countercation A in ternary oxides such as AMO_3 by a countercation with charge one less than A. UHV annealing will always tend to induce oxygen loss and thus to decrease the room temperature conductivity. In fact some of the superconducting cuprate phases will even lose oxygen at room temperature. The optimal sample preparation for materials of this sort therefore involves cleavage in UHV, possibly at low temperature to minimise oxygen loss. This type of sample preparation has proved necessary to obtain reliable photoemission spectra of conducting cuprate phases such as $YBa_2Cu_3O_7$ and La_2CuO_4 that are less robust than $Bi_2Sr_2CaCu_2O_8$, and low temperature cleavage in microscopes with cryogenic capabilities has allowed true atomic imaging of $YBa_2Cu_3O_7$.[68,69]

If the problem of sample conductivity of bulk oxide crystals at room temperature proves intractable, it may be possible to carry out the STM measurements at elevated temperatures where the conductivity is enhanced. There are obvious problems of thermal drift at high temperature, but a new generation of commercially available STM instruments allows fairly routine measurements at temperatures up to 1500 K. High temperature atomic scale imaging has been achieved on a cleaved NiO(100) surface at 473 K (Fig. 3);[90] and on $UO_2(111)$[91] and $UO_2(110)$[92] at 573 K, both oxides having insufficient room temperature conductivity to allow stable tunnelling.

Another alternative is to completely circumvent the problem of conductivity by growing a thin epitaxial oxide layer on a metal substrate. Freund *et al.*[2] have provided a recent definitive review of this area and identify three distinct approaches. The first involves simple oxidation of a metal. For example, NiO(100) can be grown by oxidation of Ni(100),[93] and $Cr_2O_3(0001)$ on Cr(110).[94] The oxide layers are often highly strained owing to mismatch with the metal. However, atomically resolved STM has been performed on Cr_2O_3 on Cr(110)[95] and on NiO(100) grown on Ni(100).[93] The second approach involves evaporation of a metal onto a metal substrate, followed by oxidation of the deposit: the metals need not be the same and therefore there is a possibility of lattice matching the target oxide to the metal substrate. Oxide surfaces prepared in this way and subsequently studied by STM include NiO(111) on Au(111),[97] FeO(111) on Pt(111),[98] $TiO_2(001)$ and MgO on Mo(100),[99] and $Al_2O_3(0001)$ on Re(0001).[98] In the last of these studies the oxide layers were used as substrates for deposition of Au, Pd and Ni metal particles in an attempt to prepare model supported metal catalysts.[98] Thirdly and finally, oxide layers can be grown by oxidation of alloys. One system of particular note in this context is oxidised NiAl(110), which yields very well ordered Al_2O_3 films two atomic layers thick.[99,100] The symmetry of the overlayer in relation to the substrate allows the existence of domains whose basis vectors are rotated by 24° relative to each other. The periodicity within the overlayer is commensurate with the NiAl(110) substrate along the $(1\bar{1}0)$ direction but incommensurate along (001). This gives rise to antiphase domain boundaries within the rotational domains. These complex surfaces have proved amenable to high quality STM imaging, which at low sample biases of the order of 30 meV reveals atomic structure within the surface unit cell.[100] The oxide overlayers have been used in turn as substrates for deposition of Pd, Pt and Rh.[99,101,102] At

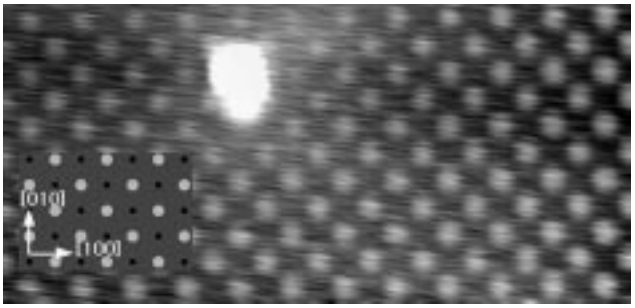

Fig. 3 Empty state STM image (+0.7 V sample bias, 1.0 nA tunnel current) of NiO(001) taken at about 473 K. The square array of greyscale maxima are believed to correspond to the Ni positions. Reproduced with permission from ref. 90.

90 K Rh nucleates randomly on the Al_2O_3, but at 300 K there is preferred nucleation at the antiphase domain boundaries.[102] Whilst this is an interesting observation in itself, it does highlight the point that non-commensurate oxide overlayers may show subtle differences in their surface properties from true bulk oxide surfaces which do not exhibit these substrate induced defects.

3.2 UHV *versus* ambient conditions

Model studies of oxide single crystal surfaces using electron based techniques such as X-ray and UV photoemission, low energy electron diffraction (LEED) and electron energy loss spectroscopy (EELS) are invariably carried out under UHV conditions. Vacuum conditions are necessary to prevent interference of gas phase molecules with electrons in their passage through the electron optics, but the more stringent need for ultrahigh vacuum arises mainly from the necessity to maintain surface cleanliness. On the other hand the technique of STM does not in itself impose requirements as to the medium in which it is applied. STM studies in both UHV and under ambient conditions therefore become a possibility, provided that sample cleanliness can be maintained in the latter.

Oxides with a layer structure held together by weak van der Waals forces usually present chemically inert cleavage planes; for example, water only weakly physisorbs onto the (001) surface of $Bi_2Sr_2CaCu_2O_8$. Layered materials are therefore particularly favourable prospects for air STM and indeed the quality of atomically resolved images obtained under ambient conditions from materials including $Bi_2Sr_2CaCu_2O_8$,[7,55,58,61] $Tl_2Ba_2Ca_2Cu_3O_{10}$[8,9,62,63] and $Pb_2Sr_2(Ca,Y)Cu_3O_8$[64] are comparable to those obtained under UHV. Rohrer and coworkers[85] have extended atomically resolved ambient STM and AFM to the non-cuprate oxides V_2O_5 and V_6O_{13}. To minimise water adsorption it is also possible to carry out the STM experiment in a closed environment glove box, although even if H_2O and CO_2 levels are reduced to the ppm level oxide surfaces will suffer huge exposures to these gases by the normal standards of UHV experiments.

The mechanism of imaging layered materials in air has aroused considerable controversy and in some cases at least it is probable that the tip makes direct contact with the sample. The apparent topographic contrast arises from 'sliding' of a raft of material across the surface with Moire type modulation of the conductivity as the top layer falls in and out of registry with the underlying layers.[103] However, a recent study by Smith and Rohrer has demonstrated that both air and UHV STM images of the layered material $Mo_{18}O_{52}$ reveal similar topographic features with similar corrugation.[89] It was also demonstrated that it was possible to obtain air STM images for Mo_8O_{23} and Mo_4O_{11} which have 3D structures derived from the ReO_3 structure rather than from the layer structure of MoO_3. An air stable (6×2) reconstruction has also been identified on the cubic perovskite $SrTiO_3$.[82] Nonetheless it is remarkable that atomically resolved STM images have apparently been obtained in air from $YBa_2Cu_3O_7$,[65,66] given that this material reacts rapidly on a macroscopic scale with both CO_2 and H_2O. In this case it impossible to believe that the image could arise from true tunnelling across an air gap to an atomically clean surface.

4 STM of tungsten oxides

4.1 Introduction to WO_3 and Na_xWO_3

Tungsten trioxide (WO_3) is a $5d^0$ transition metal oxide. The idealised structure is based on a cubic ReO_3-like framework of corner sharing WO_6 octahedra. However, tilting and distortion of the WO_6 octahedra results in deviations from the ideally cubic structure. At room temperature the bulk structure is monoclinic, with lattice parameters that essentially represent a $2\times2\times2$ superstructure on an idealised cubic unit cell of 3.7 Å. However, for the present purposes we can treat WO_3 as if it were cubic. The bandgap is about 2.6 eV at 300 K, but the bulk solid state properties are determined by the propensity of the material to become oxygen deficient WO_{3-x}. For O vacancy concentrations in excess of $x=1\times10^{-4}$ point defects are eliminated by the formation of well defined shear planes consisting of edge sharing WO_6 octahedra running along the $<1m0>$ directions.

The WO_3 structure is based on a sequence of ionic planes with stoichiometries $\{O\}$–$\{WO_2\}$–$\{O\}$ and formal ionic charges $\{2^-\}$–$\{2^+\}$–$\{2^-\}$ (Fig. 4). However, a repeating dipolar sequence such as this normal to a surface gives rise to an infinite surface energy. This precludes termination of WO_3 in either a $\{O\}$ or a $\{WO_2\}$ surface plane. However, if the final WO_2 plane is covered in half a monolayer of oxygen, the sequence $\{O_{0.5}\}$–$\{WO_2\}$–$\{O\}$ has formal ionic charges $\{1-\}$–$(2+\}$–$\{2-\}$which can be bracketed into the repeating quadrupolar sequence $(\{1-\}$–$\{2+\}$–$\{1-\})$–$(\{1-\}$–$\{2+\}$–$\{1-\})$ with the 2− charge of the subsurface $\{O\}$ layers split between two quadrupolar units. This sequence avoids a divergent surface energy. Two possible simple arrangements of half a monolayer of oxygen ions on top of a WO_2 layer can be envisaged. A situation in which oxygen ions are present on alternate W ions along the [100] and [010] directions will

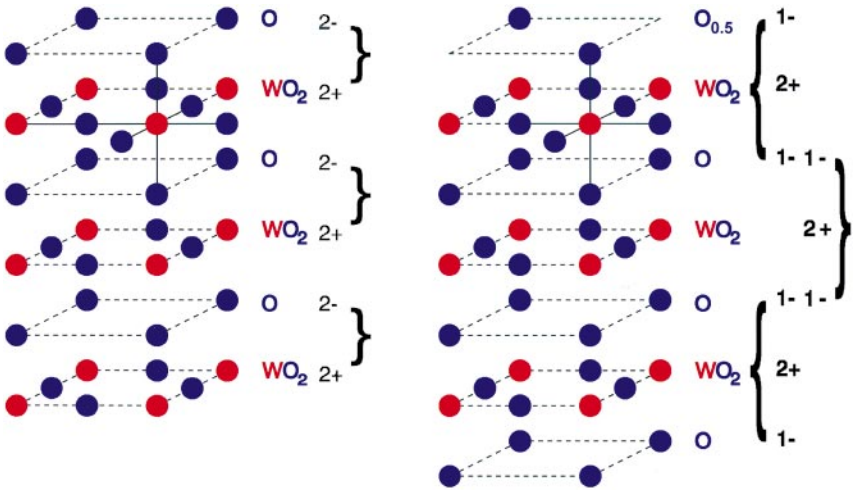

Fig. 4 The idealised cubic ReO_3 structure of WO_3, shown in terms of a sequence of charged ionic planes. The termination on the left has a repeating dipole normal to the surface and an infinite surface energy. Removal of half a monolayer of on-top O allows termination with a repeating quadrupolar charge sequence which no longer has an infinite energy.

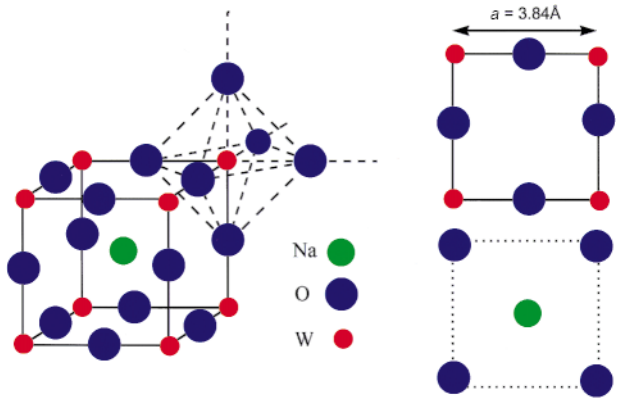

Fig. 5 The cubic perovskite structure of Na_xWO_3, showing two possible terminations for the (001) surface . The lattice parameter corresponds to $x=0.665$.

give rise to a $(\sqrt{2}\times\sqrt{2})R45^\circ$ reconstruction. Alternatively, the presence of oxygen ions on alternate rows of tungsten ions along [100] or [010] directions will give a (2×1) or (1×2) reconstruction. The energies associated with the two alternative superstructures have been calculated using atomistic modelling techniques to be 1.39 J m^{-2} and 1.67 J m^{-2} respectively.[11,12] Thus a $(\sqrt{2}\times\sqrt{2})R45^\circ$ termination is to be anticipated.

Introduction of sodium atoms into the WO_3 lattice results in a series of prototype oxide bronzes. These have the general formula Na_xWO_3 where $0.0<x<0.9$. They are of particular interest as their structural and electronic properties vary with sodium content. For low values of x the sodium tungsten bronzes retain the monoclinic structure of WO_3 and they are semiconducting. However, for x values greater than 0.43 they adopt an essentially cubic perovskite structure, based on a cubic framework of corner sharing WO_6 octahedra, with the sodium atoms occupying a fraction of the twelve-coordinate interstitial sites of the host lattice (Fig. 5). Again the structure can be described as a series of layers stacked along [001] with stoichiometries $\{Na_xO\}$–$\{WO_2\}$–$\{Na_xO\}$–$\{WO_2\}$. The Na 3s levels lie about 10 eV above the bottom of the W 5d conduction band[104] and each Na ion therefore donates one electron into the set of W 5d levels of local t_{2g} symmetry. For x values in excess of 0.26 the bronzes are metallic with conductivities approaching that of copper in the cubic regime. In the cubic metallic regime the occupied part of the conduction band is about 1 eV wide and has a nearly free electron like shape. Photoemission spectroscopy reveals the expected non-vanishing density of states at the Fermi energy. Early surface structural work on (001) surfaces of sodium tungsten bronzes identified (2×1) and (3×1) reconstructions, which were attributed to sodium ordering. The periodicity was a function of sodium content.

Taken together WO_3 and the metallic bronzes Na_xWO_3 are of particular interest in that they provide a pair of materials in which to explore the influence of a non-metal to metal transition on the scope of STM.

4.2 STM of WO_3(001)[10–14]

After annealing (001) oriented crystals of WO_3 in low (10^{-5} mbar) partial pressures of oxygen a high degree of surface order is achieved, as gauged by LEED. Stable tunnelling can only be achieved at positive sample bias typically between +1.5 V and +2 V, as expected for an n-type semiconducting oxide with the Fermi level pinned close to the conduction band minimum by d^1 states associated with oxygen vacancies.[10,11] Typical images showed large flat terraced areas supporting the expected $(\sqrt{2}\times\sqrt{2})R45^\circ$ reconstruction (Fig. 6). However, a striking feature of the images is that the terraces are dissected by defect troughs running across them. These

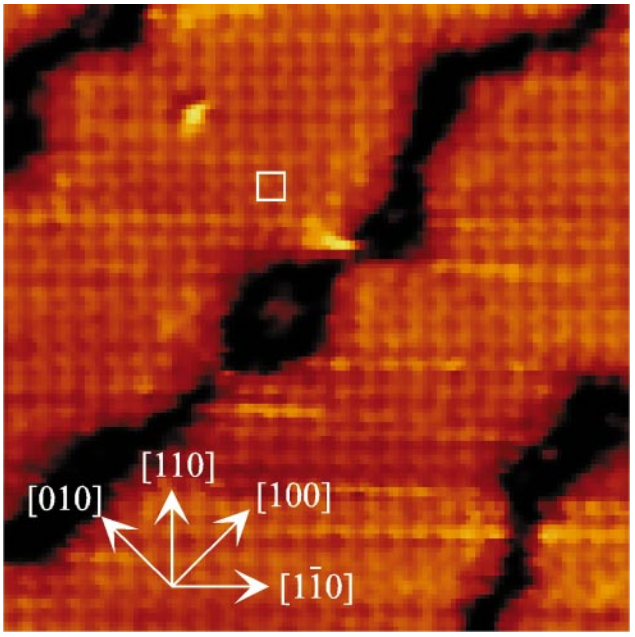

Fig. 6 130 Å × 130 Å STM image of WO_3(001) acquired at 1 nA tunnel current and +1.5 V sample bias. The $(\sqrt{2}\times\sqrt{2})R45^\circ$ unit cell is shown. Note the dark defect troughs running through the image. Adapted from ref. 11.

seem to display a quasi-periodic distribution and are constrained approximately to the [100] or [010] directions, although the troughs meander somewhat in direction and have ragged edges.

At an unrelaxed surface the on-top O ions sit about 1.9 Å above the W ions of the WO_2 plane. Atomistic simulations suggest that the on-top oxygen ions relax inward and the underlying W ions relax outward, shortening the bond length by 0.5 Å.[12] The 'bare' W ions also relax inward by 0.19 Å so that the height difference between on-top O and 'bare' W is reduced to 1.6 Å. The conduction band states in WO_3 are of dominant W 5d atomic character but there is significant mixing with O 2p states, which becomes stronger the higher the energy above the bottom of the conduction band. The bulk band structure calculations of Bullett[105] on monoclinic WO_3 give an O 2p/W 5d ratio of 0.17 for states 1.5 eV above the bottom of the conduction band. Through eqn. (6) and assuming a local barrier height of 2 eV one can estimate that this ratio gives a reduction in the apparent height difference between W and O of 1.2 Å. Thus in this case structural effects should dominate over electronic structure effects and greyscale maxima correspond to the on-top oxygen.

Consider next the defect troughs. The apparent depth of the troughs was generally found to be of the order of 2 Å which corresponds roughly to the bulk W—O bond length of 1.9 Å. Spatially resolved measurements of dI/dV *versus* V curves on a trough dissected surface are shown in Fig. 7.[14] In contrast to the regular terraces, there is substantial tunnelling from filled states at biases above 1 eV when the tip is in the proximity of a defect trough. For this reason it is believed that defect troughs are associated with areas where the $O_{0.5}$ on-top oxygen is missing to give termination in a bare WO_2 plane. Electrical neutrality is maintained if the surface W ions are reduced to W^V to give ions with a localised $5d^1$ electron configuration. Localised electron states are observed in photoemission spectra from oxygen deficient WO_3 surfaces at binding energies above about 1 eV.

To further explore the effects of oxygen deficiency, WO_3(001) $(\sqrt{2}\times\sqrt{2})R45^\circ$ was deliberately modified by argon ion bombarding and then annealing in UHV.[11,13,14] Argon ion bombardment of oxide surfaces is known to result in preferential

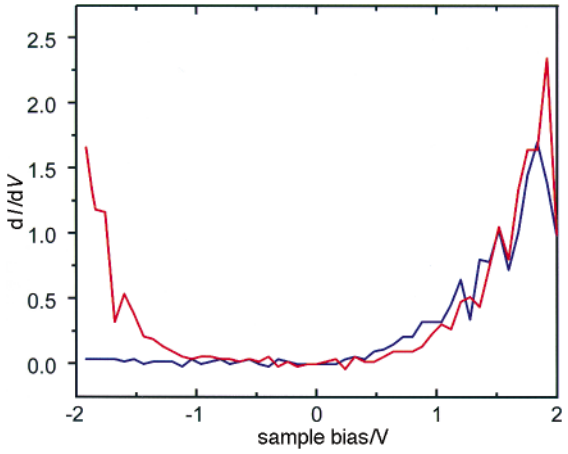

Fig. 7 Differential conductance spectra for a $WO_3(001)$ surface displaying a $c(2\times2)$ terrace reconstruction dissected by defect troughs. Blue line: on terraces. Red line: on troughs. The tip was stabilised at 1 nA tunnel current at +2.0 V sample bias at each pixel point. The feedback loop was then disengaged to measure the *I–V* curves. Each curve is derived from 20 points within an image. Adapted from ref. 14.

sputtering of oxygen from the surface. The first effect observed in the STM was the formation of new line defects on terraces which otherwise retain the original periodicity. These new linear defects are narrower and shallower than the original troughs and adhere strictly to the [100] and [010] directions. With more prolonged reduction, the two types of defect structure are observed to merge on regions of the crystal surface producing striking branched patterns and the terraces now exhibit a $p(2\times2)$ periodicity (Fig. 8). This reconstruction is believed to correspond to a situation in which half the original on-top oxygen ions have been removed to leave a WO_2 layer terminated by just a quarter of a monolayer of oxygen ions. This is necessarily accompanied by reduction of half the surface W cations from W^{VI} to W^{V}. Atomic scale filled state imaging was possible for the $p(2\times2)$ reconstruction. The reduced W^{V} ions in the (2×2) structure support localised filled electronic states close to the Fermi energy, thus enabling filled state imaging.

After further ion bombardment and anneal cycles, a further new reconstruction emerges with (1×1) periodicity.[13,14] This is confined to bright strips apparently lying 2–3 Å above the underlying terraces (Fig. 9). Similar structures were observed on surfaces that were prepared simply by annealing *in vacuo* for long periods at 700 °C. The (1×1) periodicity is clearly seen in high resolution empty state images of a vacuum annealed surface (Fig. 10). The arrangement of the atomic rows along [010] and [100] implies that the reconstruction corresponds either to a situation where all of the W ions in the WO_2 plane are capped by on-top oxygen ions, or alternatively that all of the on-top oxygens have been removed and the maxima are the W ions in the bare WO_2 layer. Since ion bombardment or high temperature annealing results in pro-

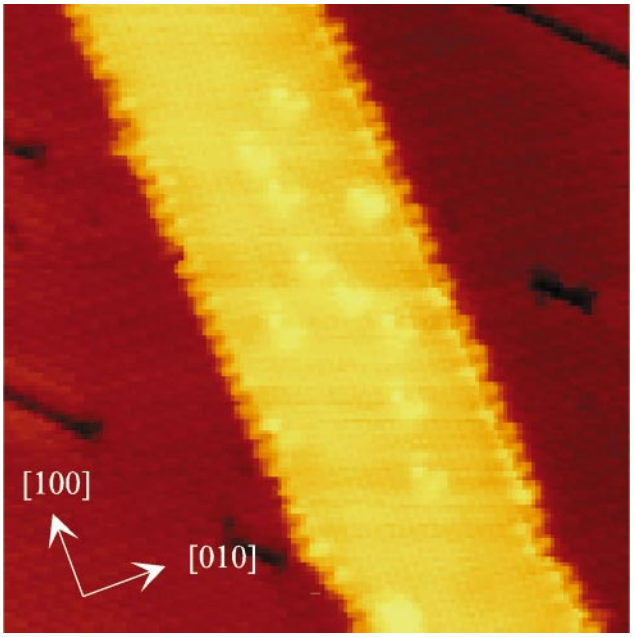

Fig. 9 280 Å × 280 Å STM image of $WO_3(001)$ acquired at +1.5 V sample bias and 1 nA tunnel current after several prolonged cycles of ion bombardment and annealing. The bright raft running across the image supports a (1×1) reconstruction. The darker areas support a $p(2\times2)$ reconstruction. Adapted from ref. 14.

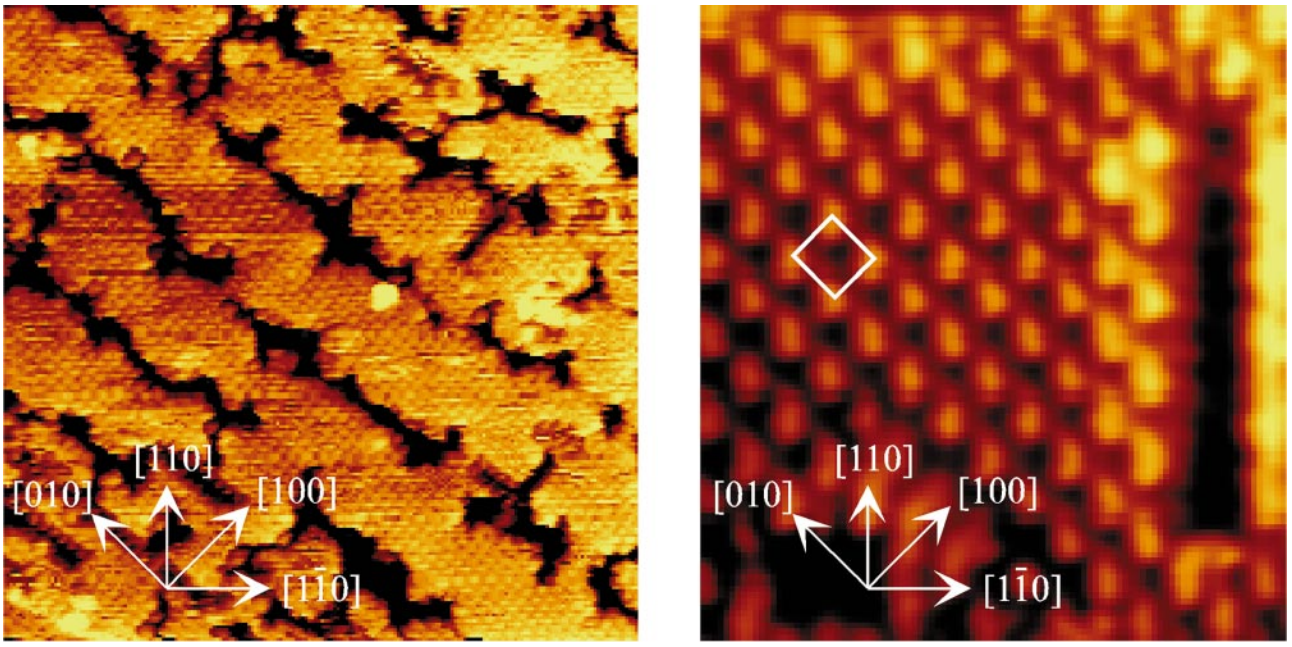

Fig. 8 Left hand panel: STM images after bombardment of $WO_3(001)$ by 500 eV argon ions at 6 μA for 60 min followed by UHV annealing at 700 °C overnight. +2.0 V sample bias, 1 nA tunnel current. Note branched defect structure. Right hand panel is a high resolution scan of typical terrace structure corresponding to image on left. The new $p(2\times2)$ unit cell is highlighted. Adapted from ref. 11.

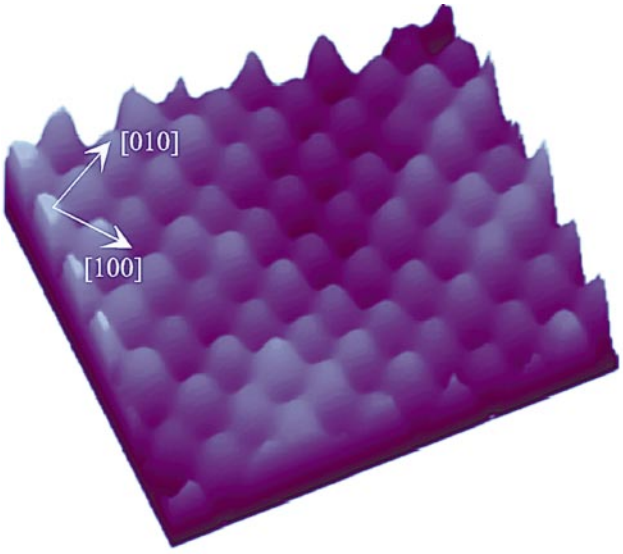

Fig. 10 3D rendering of high resolution image of (1×1) reconstruction on $WO_3(001)$: 1 nA, +1.2 V sample bias. Adapted from ref. 13.

gressive removal of oxygen ions, it is more likely that the image is that of bare W ions. This is supported by XPS data which show a progressive decrease in the O/W ratio as one moves through $(\sqrt{2} \times \sqrt{2})R45^\circ$, $p(2 \times 2)$ and (1×1) reconstructions. Removal of the on-top oxygen ions from the WO_2 layer leaves behind electrons, resulting in reduction of the tungsten ions from W^{VI} to W^{V}. Thus, although the ionic layers have stoichiometries $\{WO_2\}$–$\{O\}$–$\{WO_2\}$–$\{O\}$, the formal charges on the planes will be $\{1+\}$–$\{2-\}$–$\{2+\}$–$\{2-\}$ which can be grouped into the quadrupolar sequence $\{(1+)$–$(2-)$–$(1+)\}$–$\{(1+)$–$(2-)$–$(1+)\}$. This avoids the divergent surface energy associated with a repeating dipole at the surface.

A further consequence of the reduction of the W ions on oxygen loss is the enhanced amenability of the (1×1) structure to filled states imaging as compared to the larger periodicity reconstructions. Imaging at negative sample biases is still highly unstable and usually of short duration, but it is nonetheless possible and gives higher quality images than those achieved for the $p(2 \times 2)$ reconstruction. Fig. 11 shows a filled states image of the vacuum annealed surface taken at a sample bias of −0.4 eV. The average periodicity measured along the [100] and [010] directions matches that measured from empty state images. The maxima in the images again correspond to the positions of the reduced W^{V} cations. The electron density associated with these cations now allows a significant tunnelling current to flow at negative sample biases.

In summary, WO_3 surfaces show a range of oxygen stoichiometries which give rise to at least three surface reconstructions. The evolution between these reconstructions involves well defined defect structures in which oxygen vacancies demonstrate a marked propensity to aggregate. This behaviour in many ways parallels the aggregation of bulk defects to give crystallographic shear planes.

4.3 STM of $Na_xWO_3(001)$[15–17]

Two groups have studied STM of (001) surfaces of sodium tungsten bronzes. In our own STM experiments[16,17] we have concentrated on a single sodium content $Na_{0.665}WO_3$ and have characterised two different reconstructions. Annealing at high temperatures in UHV between 650 and 800 °C gives surfaces exhibiting a $(\sqrt{2} \times \sqrt{2})R45^\circ$ reconstruction, but lower annealing temperatures yields a (2×1) surface.

STM imaging of high temperature annealed sodium tungsten bronzes can be performed over a wide range of sample biases

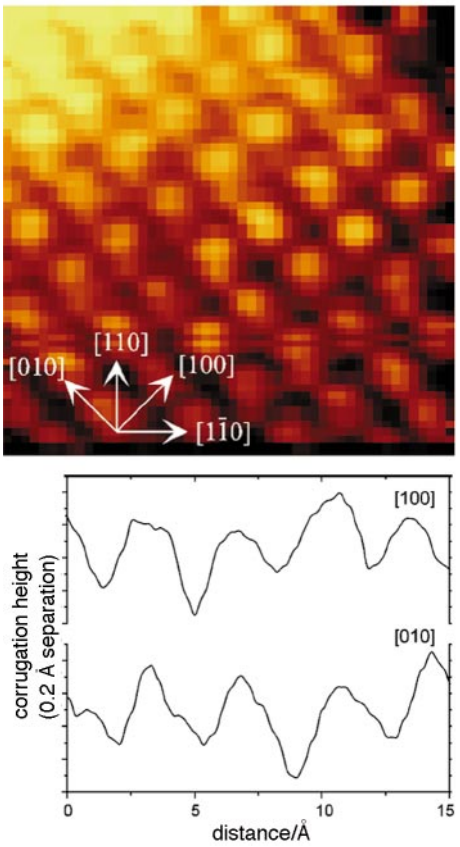

Fig. 11 (Top) filled state STM 25 Å × 25 Å image of 1×1 reconstruction on $WO_3(001)$ taken at 1 nA tunnel current and −0.4 V sample bias. (Bottom) corrugation profiles along the [010] and [100] directions. Adapted from ref. 13.

between −2.0 V and +2.0 V. This is to be expected for a metallic material. Fig. 12 shows a pair of images taken at +0.6 V and −0.6 V sample bias acquired simultaneously by switching the voltage between forward and reverse travels of the x piezo drive. The periodicity in the square array of greyscale maxima is characteristic of the $(\sqrt{2} \times \sqrt{2})R45^\circ$ reconstruction. By analogy with WO_3 it is probable that this reconstruction arises from an ordered array of on-top oxygen ions in a $O_{0.5}$ surface plane. Na ions may be confined to subsurface planes, although it is hard to establish this definitively. Again we consider that we are imaging oxygen ions, rather than the W ions on which the density of states at the Fermi energy is mainly localised. Owing to covalency the electronic states at the Fermi level again have something of the order of 15% O 2p atomic character and this coupled with the fact that the on-top O ions sit more more than 1.5 Å above the WO_2 plane allows the O ions to appear as the maxima. Filled state images are very similar to the empty states images in displaying a square array of greyscale maxima. However, it is additionally possible to discern extra spots in the centre of the squares. In fact, these subsidiary maxima are also present in the filled states image, but are less well defined. This is clarified by comparison of the corrugation profiles taken along the [100] direction from the filled and empty states images. On average, the maxima are 0.05 Å above the minima in +0.6 V empty state images, but 0.09 Å above the minima in −0.6 V filled state images. For comparison, the dominant maxima are 0.20 Å above the minima in empty state images and 0.21 Å above the minima in filled state images. In our model, the subsidiary maxima correspond to bare W ions in the WO_2 plane. The variation in the height of the maxima with bias voltage can be understood in terms of the density of states ratio. The O contribution to the density of states decreases on moving down the conduction band and for a

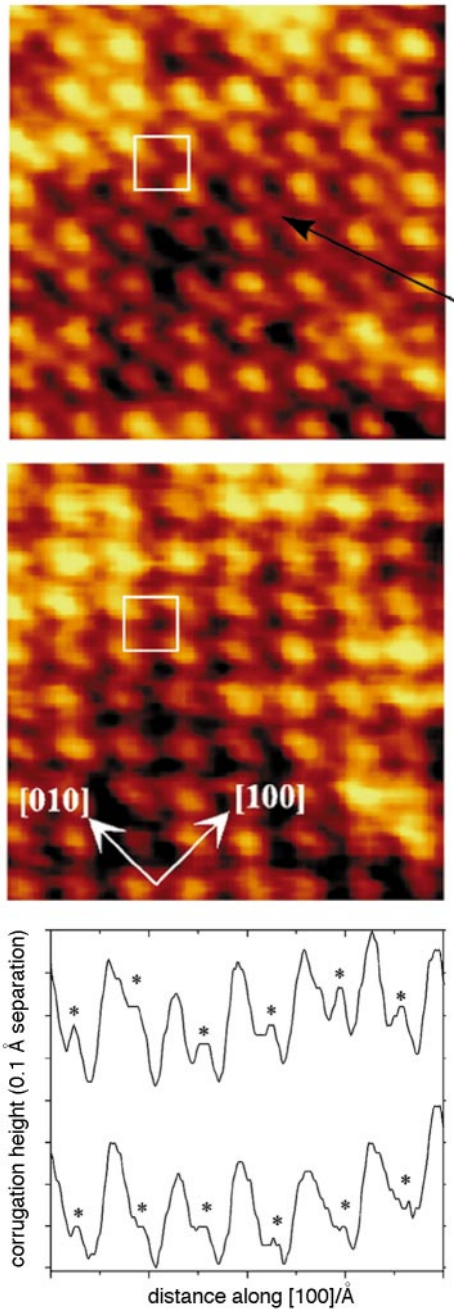

Fig. 12 (Top) 40 Å × 40 Å STM images of $(\sqrt{2}\times\sqrt{2})R45^\circ$ reconstruction on $Na_{0.665}WO_3(001)$ taken at 1 nA tunnel current and −0.6 V sample bias (upper) and +0.6 V sample bias (lower). The [110] direction runs vertically. The $(\sqrt{2}\times\sqrt{2})R45^\circ$ unit cell is highlighted. Note square array of greyscale maxima with subsidiary maxima in the upper panel. (Bottom) corrugation profiles along [100] which reveal subsidiary maxima in both images. Adapted from ref. 16.

perfectly cubic perovskite there can in fact be no mixing at the bulk Γ point at the bottom of the band. Thus in filled state images where one is tunnelling predominantly from electronic states 0.6 eV below the Fermi energy (and therefore only about 0.4 eV above the conduction band minimum), the bare W atoms make an enhanced contribution with respect to the on-top oxygen ions.

Large area STM images of the tungsten bronze $(\sqrt{2}\times\sqrt{2})R45^\circ$ reconstruction were notably free of anything corresponding to the trough defects of WO_3. However, antiphase boundaries were imaged as a displacement of the maxima by 2.7 Å along the [110] direction. The displacement occurs abruptly in a single $\sqrt{2}$ unit cell.

Delicate optimisation of annealing conditions below 650 °C allows preparation of a (2×1) reconstruction[17] without switch over to the high temperature $(\sqrt{2}\times\sqrt{2})R45^\circ$ reconstruction described above. As expected, LEED implies the presence of 90° rotated (2×1) and (1×2) domains. Again STM imaging was possible over a wide range of sample biases. STM showed that the nominally ordered (2×1) surface contained many areas where the atomic ordering is in fact far from perfect, although orthogonal (2×1) and (1×2) domains were observed in many images.

A high resolution STM image is shown in Fig. 13. The unreconstructed (001) surface would be expected to display a square array of topographic maxima, but the image clearly shows a doubling of the periodicity along the [100] direction, with rows of double maxima running along [010]. Some intensity is apparent between the rows, although it should be noted that such intensity was not always observed. The images obtained in our work show considerably greater anisotropy than those previously obtained by Rohrer and coworkers.[15] Line profiles taken along the atomic rows clearly demonstrate the (2×1) periodicity. The average periodicity along [010] is 3.8 Å (the lattice parameter for $x=0.665$ is 3.839 Å), and the corrugation height 0.49 Å. The average periodicity along [100] is 7.7 Å (twice the lattice parameter), with alternating separations of 2.2 Å and 5.5 Å between adjacent maxima. The weak features between the dimer rows are 0.46 Å above the minima.

The observed lateral relaxation is so extreme that there is no obvious way of correlating the images with the ionic packing of a WO_2 surface plane. However, the images are easily understood in terms of an $Na_{0.5}O$ termination. Displacement of the oxygen ions by 0.8 Å along [100] doubles

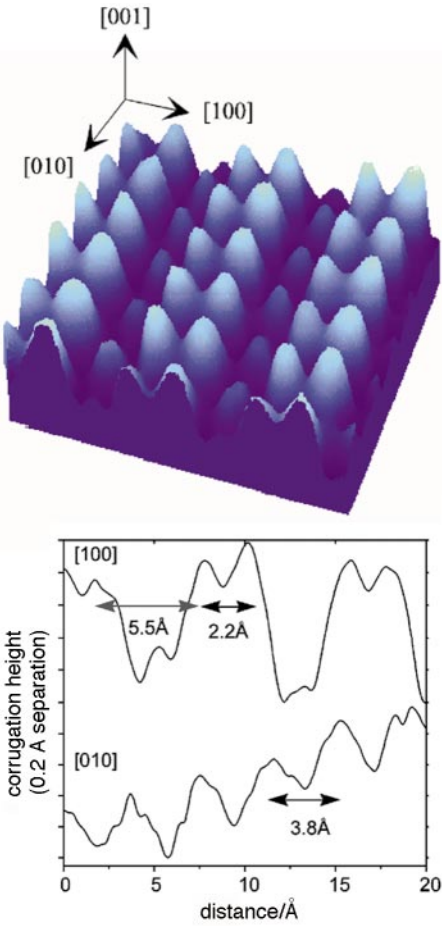

Fig. 13 (Top) high resolution 'false' 3D view of $Na_{0.665}WO_3(001)$ from STM image acquired at 1 nA tunnel current and −0.4 V sample bias showing dimer structure within the (2×1) unit cell. Note also weak intensity between the dimer rows. (Bottom) corrugation profiles corresponding to the high resolution image. Adapted from ref. 17.

the surface periodicity in this direction. The weak intensity between the dimer rows is then attributed to ordered Na^+ ions. This is shown schematically in Fig. 14. The imaging of Na^+ ions is unexpected in terms of electronic structure arguments, because the density of Na states close to the Fermi energy is very small. However, other mechanisms for creation of apparent topographic contrast may be operative, such as variation in the local barrier height. An apparent problem is that the O—O separation within the dimeric surface species (2.2 Å) is significantly less than twice the ionic radius of the O^{2-} ion [$2r(O^{2-})=2.8$ Å], suggesting incipient bonding between the ions. A dimer consisting of two O^{2-} ions would have the formal valence electron configuration $\sigma_g^2\pi_u^4\pi_g^4\sigma_u^2$. Close approach of the O^{2-} ions will raise the upper antibonding σ_u orbital. Movement of this level above the Fermi level must result in transfer of electron density out of the orbital. In the limit of complete electron transfer, the surface dimer thus approximates to the peroxide species O_2^{2-} with the electron configuration $\sigma_g^2\pi_u^4\pi_g^4$. However, the O—O bond length of a true peroxide anion (*e.g.* 1.49 Å in Na_2O_2) is considerably shorter than the O—O separation measured from the STM image, implying that the transfer of electron density is incomplete. Consideration of the origin of the $(\sqrt{2}\times\sqrt{2})R45^\circ$ reconstruction observed at high temperatures provides insight into the driving force behind such electron transfer. In the former case, the high surface energy associated with an O surface layer (formal charge 2−) on top of a WO_2 layer (formal charge 2+) is reduced by removal of half the surface O^{2-} ions, generating the reconstruction. Dimerisation of oxygen ions, accompanied by transfer of electron density, provides an alternative mechanism for the reduction of surface charge without loss of oxygen ions.

In summary, the sodium tungsten bronzes show the tunnelling characteristics of a metal and both filled and empty state imaging can be performed. Two different reconstructions have been identified, both arising from the need to reduce the charge in the outermost ionic layer. The $(\sqrt{2}\times\sqrt{2})R45^\circ$ reconstruction is very similar to that on $WO_3(001)$, but the (2×1) reconstruction has no analogue in the parent material. Another major difference between the two materials is that Na_xWO_3 surfaces show a much less rich defect chemistry, with no indication of the cooperatively organised line defects that are characteristic of WO_3. In some ways this simply mirrors the bulk defect chemistry: the metallic bronzes have no propensity toward accommodating the intriguing shear plane defects that are found in WO_3. This in turn reflects the fact that sodium doping brings about chemical reduction of the WO_3 framework and there is a less strong driving force for reduction by oxygen loss.

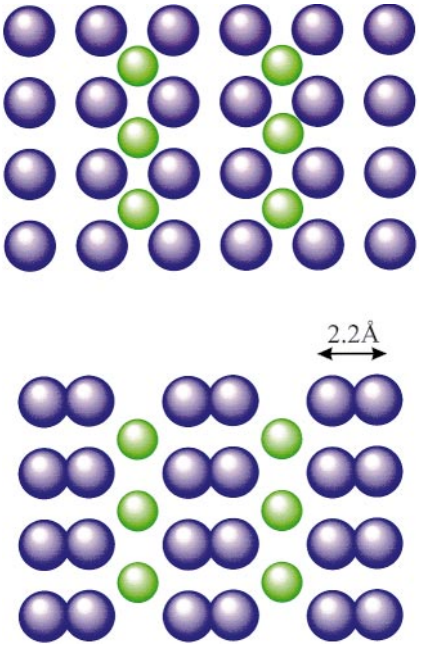

Fig. 14 Schematic representation of the $Na_{0.5}O$ terminated $Na_{0.665}WO_3(001)$ (2×1) surface. Small spheres are Na^+, large spheres are O^{2-}, assigned their conventional ionic radii. The upper panel shows the unrelaxed structure, the lower panel the structure inferred from STM. The oxygen ions are seen to overlap in the latter. Adapted from ref. 17.

5 STM of TiO_2

5.1 Background

Titanium dioxide is of enormous industrial importance as a white pigment, but there is also interest in application of the material as a catalyst or catalyst support; in photocatalytic devices; and as a gas sensor. Moreover, single crystals of the rutile form of TiO_2 are perhaps more easily and cheaply available than for any other conducting metal oxide. For these and other reasons TiO_2 has been the object of more STM investigations than any other oxide (with the possible exception of layered cuprates). At least six groups have established their credentials in this field by obtaining images with atomic or unit cell resolution.[20–22,26,27,30] As is perhaps to be expected, controversies have arisen over both the experimental data and its interpretation.

The tetragonal rutile structure of TiO_2 is shown in Fig. 15. Viewed perpendicular to the (110) direction the rutile structure is built up of ionic planes with stoichiometry $\{O\}$–$\{Ti_2O_2\}$–$\{O\}$–$\{O\}$–$\{Ti_2O_2\}$ *etc.*, carrying formal ionic charges $\{1-\}$–$\{2+\}$–$\{1-\}$–$\{1-\}$–$\{2+\}$. A stable quadrupolar sequence of charged layers is therefore obtained if the outer $\{Ti_2O_2\}$ layer is terminated by an outer $\{O\}$ layer of oxygen ions as shown schematically in Fig. 16. These oxygen ions complete six-fold coordination of half the surface Ti cations, leaving the remaining Ti cations five-coordinate. Argon ion bombardment results in selective sputtering of oxygen, along with significant disruption of the surface. However, oxygen stoichiometry can be partially restored by low temperature annealing to give a (2×1) reconstructed surface.[107] Prior to STM experiments it was generally presumed that in this reconstruction half the rows of outer bridging oxygen ions were missing to leave four-fold coordinate surface cations as well as the original bare five-fold cations, as shown schematically in Fig. 16.

The roughly octahedral crystal field experienced by the Ti cations splits the Ti 3d conduction band into three-fold degenerate t_{2g} and two-fold degenerate e_g components. A gap of just over 3 eV separates the empty 3d states from the filled valence band of O 2p states. Oxygen deficiency introduces occupied Ti 3d donor levels just below the conduction band minimum so that like WO_{3-x}, TiO_{2-x} is an n-type semiconductor.

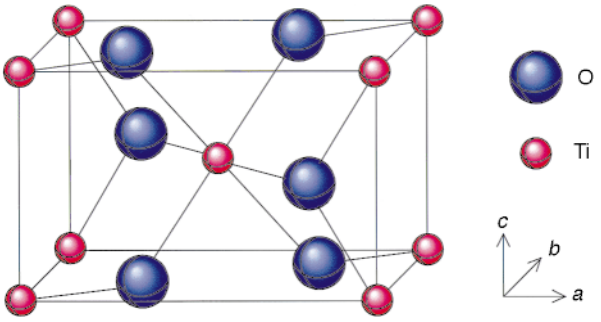

Fig. 15 The tetragonal rutile structure of SnO_2 and TiO_2

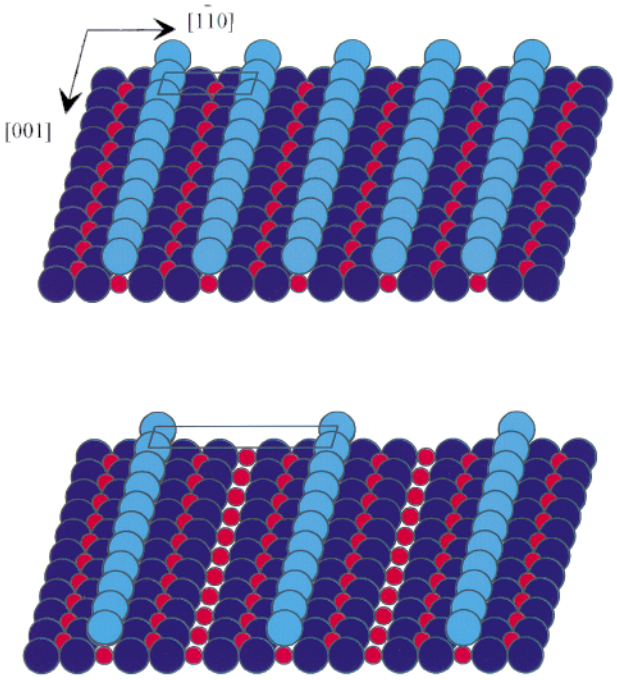

Fig. 16 Models for the (1×1) and (1×2) reconstructions on $TiO_2(110)$. Small red spheres are Ti, large dark blue spheres are O. Note the rows of on-top O, represented by light blue spheres.

5.2 STM of $TiO_2(110)$

Despite early difficulties in obtaining STM images from $TiO_2(110)$ with the periodicity expected from the bulk crystal structure,[18,19] at least 11 papers have now appeared in the literature containing unit cell resolved STM images from the (1×1) reconstructed surface.[20–30] A general feature in all of these images is a series of bright rows running along the [001] direction with the correct separation along [110] for the (1×1) reconstruction. As expected from the electronic structure, imaging of TiO_2 surfaces is most easily achieved at positive sample bias under conditions which probe empty electronic states. Since these states are of dominant Ti 3d atomic character, one interpretation of STM images assumes that the five-coordinate cation positions appear as topographic maxima. However, based on molecular orbital calculations on a $[Ti_7O_{24}]^{20-}$ cluster, Fischer *et al.* have argued that strong Ti—O covalency at TiO_2 surfaces gives rise to a substantial contribution of O 2p states to conduction band levels.[26,28] Thus whilst electronic structure effects partially offset the protrusion of the bridging O atoms, they cannot completely dominate topography. In support of this assignment it was also noted that the bright topographic rows contain a large number of vacant sites, which in the 'O imaged' model correspond to missing on-top O (Fig. 17). It is harder to account for these vacancies in the 'Ti imaged' model. However, Diebold *et al.*[30] found a different sort of characteristic image associated with defects in which additional bright features appear between the bright rows (Fig. 18). Following the same line of argument as Fischer *et al.* obviously leads to assignment of the bright rows to Ti cation positions. Evaluation of charge density contours as outlined in Section 2.3 supports this conclusion. As shown in Fig. 19 the charge density contours for empty electronic states suggest that the STM tip should image Ti cation positions as greyscale maxima, except under conditions where the tip is very close to the surface (*i.e.* with very high tunnelling current). James and coworkers[31] reached a similar conclusion from evaluation of empty state charge densities at fixed heights. At 4 Å above the surface, maximum empty state charge density is found above Ti positions, whereas 2 Å above the surface the maximum charge density corresponds to O positions. The

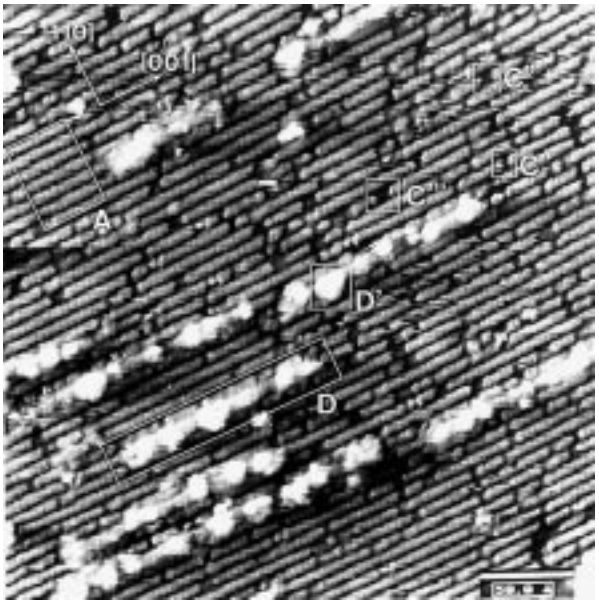

Fig. 17 Empty state image of $TiO_2(110)$ (1×1) taken at $+1.55$ V sample bias. Note bright rows running along [001] direction, with gaps (labelled C) in the rows. The rows are attributed to on-top O ions and the gaps to O vacancies. Reproduced with permission from ref. 26.

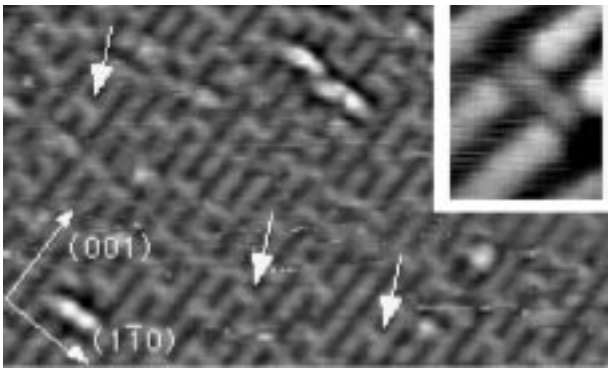

Fig. 18 Empty state image of slightly oxygen deficient $TiO_2(110)$ (1×1) taken at $+1.2$ V sample bias and 0.5 nA tunnel current. The arrows point to features believed to be O vacancies which here appear as bright features between the rows of the (1×1) reconstruction. Reproduced with permission from ref. 30.

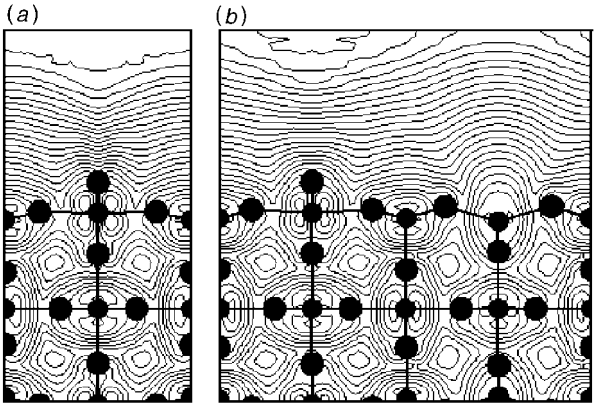

Fig. 19 Contour plots of charge density averaged along the [001] direction for empty states within 2 eV of the conduction band minimum for $TiO_2(110)$: (*a*) relaxed (1×1) reconstruction. Ti positions are at the edge of the plot; (*b*) relaxed missing row (1×2) reconstruction. Reproduced with permission from ref. 30.

theoretical work suggests that it might be possible to observe a reversal of image contrast as the tunnel current or bias is varied, thus varying the tip–sample separation.

An additional aid to assignment is provided by adsorption studies. Formate ions are expected to adsorb on surface cation sites. Onishi and coworkers obtained atomically resolved STM images from $TiO_2(110)$ that had been exposed to HCOOH.[22,23,25] Bright spots were found to decorate the bright rows, with a disordered arrangement of the adsorbate induced features at low coverage and a (2×1) ordering at higher coverage. The obvious interpretation of this data is to assign the spots to individual formate ions which are imaged *via* the LUMO of the ion. It follows that the bright rows of the underlying reconstruction correspond to Ti positions.

Interpretation of STM images from the (1×2) reconstruction has proved to be equally controversial. As discussed above, the simplest model for the (1×2) reconstruction involves missing rows of bridging O atoms, thus leaving rows of four-coordinate Ti ions between alternate pairs of rows of five-coordinate Ti. Very high resolution STM images of this surface obtained by Murray *et al.*[27] appeared consistent with this model (Fig. 20), but revealed a 0.5 Å relaxation of five-coordinate Ti ions toward the missing oxygen row, as well as a 0.25 Å inward relaxation. However, based on dynamic observation on TiO_2 surfaces under various thermal and oxygen exposure treatments, Onishi and coworkers[22,25,29] proposed an alternative model in which Ti ions diffuse to the surface to give 'added rows' of stoichiometry Ti_2O_3 (Fig. 21). The cations are not 'bare' in this reconstruction and, in agreement with this model, formate ions were found not to adsorb on the bright rows of the (1×2) reconstruction. The model also explains the observation that the double stranded rows of the (1×2) reconstruction appear to sit 2 Å above the terraces of adjacent terrace areas of the crystal surface with (1×1) periodicity. Very recent electron stimulated desorption studies support the model of added Ti_2O_3 rows.[107] If the missing row model were correct, the desorbing flux of O ions produced by electron irradiation should maximise in a single band normal

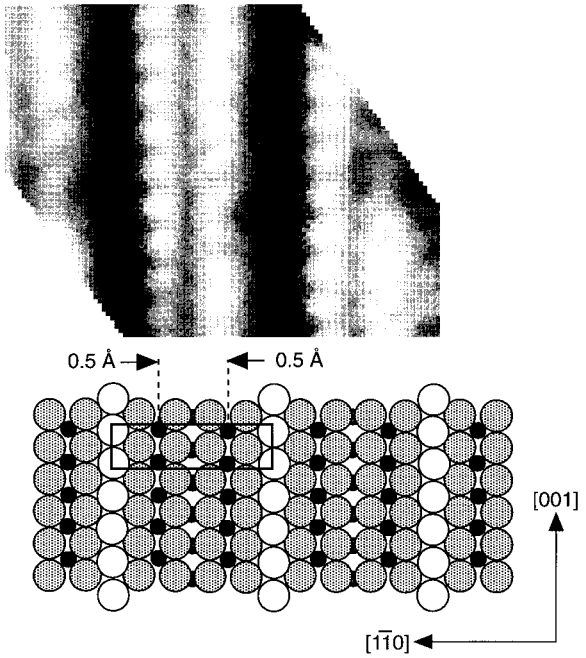

Fig. 20 High resolution empty state STM image of $TiO_2(110)$ (1×2) taken at 0.5 nA tunnel current and +1.0 V sample bias, together with a model for the surface derived from the STM image. Large open circles: on-top O. Large shaded circles: in-plane O. Small black complete circles: Ti^{4+}. Small black incomplete circles at cell centre are Ti^{3+}.The bright rows are attributed to Ti^{4+} ions and the dark rows to on-top O. Reproduced with permission from ref. 27.

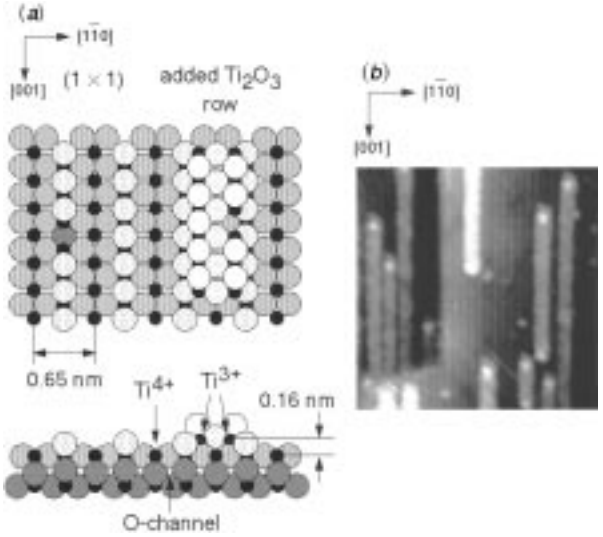

Fig. 21 (*a*) A depiction of added Ti_2O_3 rows on $TiO_2(110)$. A single O vacancy is included in the upmost O layer to allow viewing of the underlying Ti positions. (*b*) The added Ti_2O_3 may be imaged as double stranded rows in STM (image taken at +1.0 V sample bias, 0.4 nA tunnel current). Ordering of the added rows is postulated to produce the (1×2) reconstruction. Reproduced with permission from ref. 29.

to the surface. However, in the added row model O ions will desorb from the edges of the added rows to give a double banded structure with a node normal to the surface. The latter conforms with experimental observations.

5.3 STM of $TiO_2(100)$

The (100) surface of TiO_2 has a higher surface energy than $TiO_2(110)$. Ion bombardment and annealing inevitably leads to a (1×3) reconstruction. The initial model for this reconstruction again involved missing oxygen rows. This model accounted for the appearance of bandgap states in photoemission associated with reduced Ti^{3+} ions. However, a grazing incidence X-ray diffraction study suggested a more complex reconstruction involving (110) microfacets. STM provided spectacular confirmation of this model in what was probably the first atomically resolved STM study[32] of a 3D oxide (Fig. 22). To reconcile the microfacet structure with photoemission and STM observation it was, however, necessary to assume that oxygen ions were missing from the top of the ridges of the microfacet structure.[32,33] The Ti ions adjacent to these oxygen vacancies are reduced from Ti^{IV} to Ti^{III}. The reduced Ti ions act as centres for nucleation of C_{60} molecules which can be imaged directly in STM.[35]

An extension of the work on $TiO_2(100)$ examined a vicinal surface cut 2.6° off the (100) plane towards [001]. Here it was found that the vicinal off-cut steps expected along [001] induce up–down steps along [010] in which the size of the (110) microfacets is extended. This effectively replaces areas of (001) surface at the [001] steps by the lower energy (110) surface.[34]

6 STM of iron oxides

6.1 Background

Iron forms three principal oxides: haematite α-Fe_2O_3, magnetite Fe_3O_4 and wustite $Fe_{1-x}O$. The structure of α-Fe_2O_3 is based on a hexagonally close packed (hcp) array of oxygen ions within which two thirds of the octahedral holes are occupied by Fe^{III}. Fe_3O_4 by contrast has a spinel structure based on a cubic close packed (ccp) array of oxygen ions. One half of the octahedral holes and one eighth of the tetrahedral holes are occupied by iron. In contrast to 'normal' spinels where the three-valent M^{III} cations exclusively occupy the

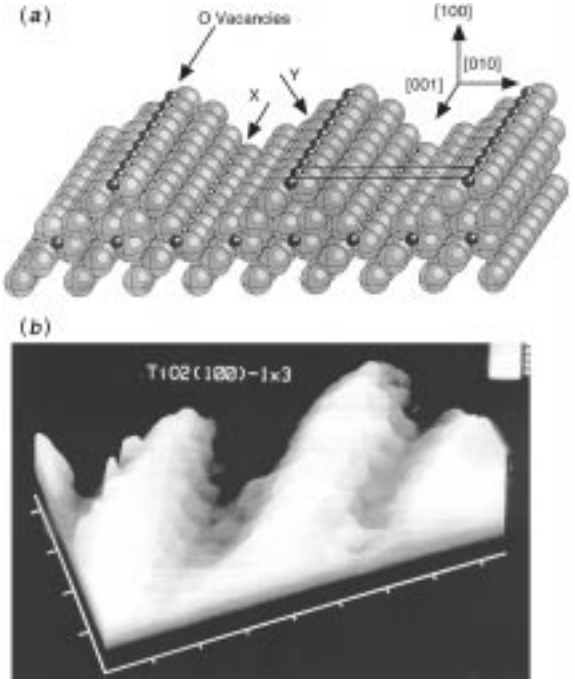

Fig. 22 (*a*) Microfacet model for the (1×3) reconstruction of $TiO_2(100)$. Large spheres are O, small spheres are Ti. The unit cell is indicated. (*b*) 3D view of the (1×3) reconstruction obtained from constant current empty state STM image taken at $+2$ V sample bias and 0.3 nA tunnel current. Reproduced with permission from ref. 34.

octahedral (O_h) sites and the two-valent M^{II} cations occupy the tetrahedral (T_d) sites, Fe_3O_4 is an inverse spinel. Half of the Fe^{III} cations occupy the T_d sites, whilst the O_h sites are occupied by both Fe^{II} and Fe^{III}. Below the Verwey transition temperature of 120 K, the Fe^{II} and Fe^{III} are partially ordered, but they probably become disordered above this temperature. $Fe_{1-x}O$ has a rocksalt-like structure, again based on a ccp array of oxygen ions. The bulk material has no range of thermodynamic stability at room temperature and disproportionates into Fe and Fe_3O_4. However, at elevated temperatures the rocksalt phase is entropically stabilised but always with a significant Fe deficiency. The Fe^{III} ions which are necessarily present in $Fe_{1-x}O$ are displaced into T_d sites within the ccp oxide array and interstitial T_d Fe^{III} and O_h cation vacancies organise into so-called Koch clusters, which introduce a structural element reminiscent of Fe_3O_4.

The Fe oxides are thus seen to be all based on close packed oxygen arrays. The O—O separation within the hexagonally packed O layers decreases progressively from 3.04 Å for $Fe_{1-x}O$ to 2.97 Å for Fe_3O_4 and 2.90 Å for Fe_2O_3. The close structural relationships between the iron oxides allows facile interconversion between the different bulk phases. Moreover, a metastable γ form of Fe_2O_3 with a ccp oxygen ion array may be prepared by careful oxidation of Fe_3O_4. This has a spinel-like structure, but with an ordered array of vacancies on the O_h iron sublattice

6.2 STM of $Fe_2O_3(0001)$

In the first UHV STM study of Fe_2O_3 an (0001) oriented single crystal was studied.[37] The cleaning procedure involved cycles of argon ion bombardment and annealing in UHV, followed by a final anneal in 10^{-6} mbar of O_2 at 1000 K. The resulting surface displayed a hexagonal LEED pattern rotated by 30° relative to crystallographic axes of α-Fe_2O_3. STM images were obtained at positive sample bias and displayed hexagonal symmetry with a 6.0 Å periodicity. These observation were consistent with a model proposed in earlier LEED studies which involved an epitaxial layer of Fe_3O_4 on top of the Fe_2O_3. The greyscale maxima in the STM images were interpreted as arising from Fe cations that would be tetrahedrally coordinated in the bulk. These occupy one quarter of the three-fold hollow sites in the hcp oxygen ion layer.

With slightly different surface preparation procedures, involving a final anneal in oxygen at 1073 K, a more complex LEED pattern is observed with floreting of the primary LEED spots by smaller spots in a hexagonal array.[38] Empty state STM images of these surfaces revealed an ordered hexagonal array of two types of mesoscopic islands with a superlattice dimension of about 40 Å (Fig. 23). From a consideration of atomically resolved structure within the islands, it was concluded that the island corresponded to regions of α-$Fe_2O_3(0001)$ and FeO(111). Somewhat surprsingly it appeared that oxygen ion positions were imaged in the former. Fourier transform of the STM images generated a pattern that displayed the same essential features as the floreted LEED patterns, thus establishing that that this structure is due to the mesoscopic 'biphase' ordering. The driving force for biphase ordering was proposed to be the small mismatch between O—O separations in FeO and Fe_2O_3, which limits the size of FeO(111) islands that can grow on $Fe_2O_3(0001)$.

6.3 STM of Fe_3O_4

The most interesting and comprehensive STM experiments on Fe_3O_4 relate to the (111) surface[42,43] which has the same hexagonal symmetry as $Fe_2O_3(0001)$. Earlier work on $Fe_3O_4(100)$[39,40] and $Fe_3O_4(110)$[41] has been reviewed elsewhere.[44]

Surface cleaning by 500 eV ion bombardment followed by annealing in UHV at 1050 K leads to surfaces displaying sharp hexagonal LEED patterns. Very high quality STM images from these surfaces were obtained at positive sample bias.[42] Two different types of terrace reconstruction, designated as type A and type B were imaged on the same crystal, with step heights of 3.8 Å down from A to B and 0.5 Å from B to A. Within the Fe_3O_4 structure there are two types of Fe containing (111) plane (Fig. 24). The first contains only Fe cations that would be O_h coordinated in the bulk. These so-called Fe_{oct2} ions occupy 3/8 of the three-fold hollow sites of the underlying close packed (111) O layer. The second type of layer contains Fe ions that would be O_h and T_d coordinated in the bulk. The Fe_{oct1} O_h ions occupy 1/8 of the three-fold hollow sites of the underlying (111) O layer. The T_d Fe ions are of two sorts. One

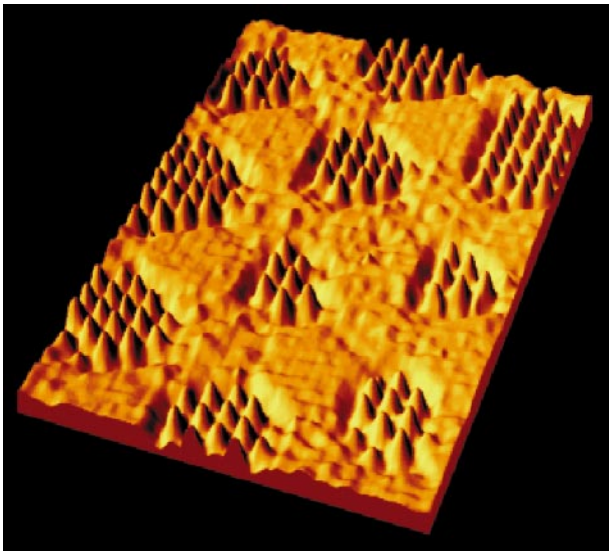

Fig. 23 A 3D rendering of an STM image of $Fe_2O_3(0001)$ taken at -2.0 V sample bias and 1 nA tunnel current. The image shows an arrangement of two types of island arranged in a mesoscopic hexagonal superlattice of dimension 40 Å. Adapted with permission from ref. 38.

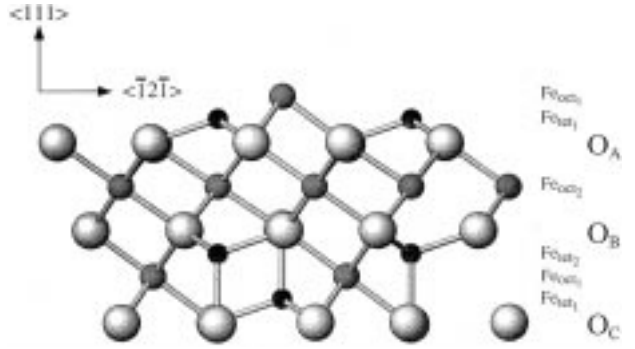

Fig. 24 A schematic representation of the structure of Fe_3O_4, showing the arrangment of the two types of Fe layers relative to the close packed O layers. Small spheres are Fe, large spheres are O. Reproduced with permission from ref. 42.

set (designated Fe_{tet1}) occupies another 1/8 of the three-fold hollow sites: in an unrelaxed bulk truncation these ions would be beneath the Fe_{oct1} ions. The other set (Fe_{tet2}) occupy 1/4 of the positions on-top of underlying O and sit above the Fe_{oct1} ions. From a consideration of the step heights and the structure within the high resolution images, the type A terraces were attributed to the Fe_{oct2} layers, with each trimer of Fe cations capped by an oxygen ion (Fig. 25). These ions could be imaged as greyscale maxima at both positive and negative sample bias. The type B images were then assigned to the second type of Fe layer. The outer ionic plane was shown to contain only Fe_{oct1} and Fe_{tet1} ions (*i.e.* ions occupying hollow sites), which were imaged as distinguishable features in the STM images only at positive sample bias.

Surfaces prepared by annealing at somewhat more elevated

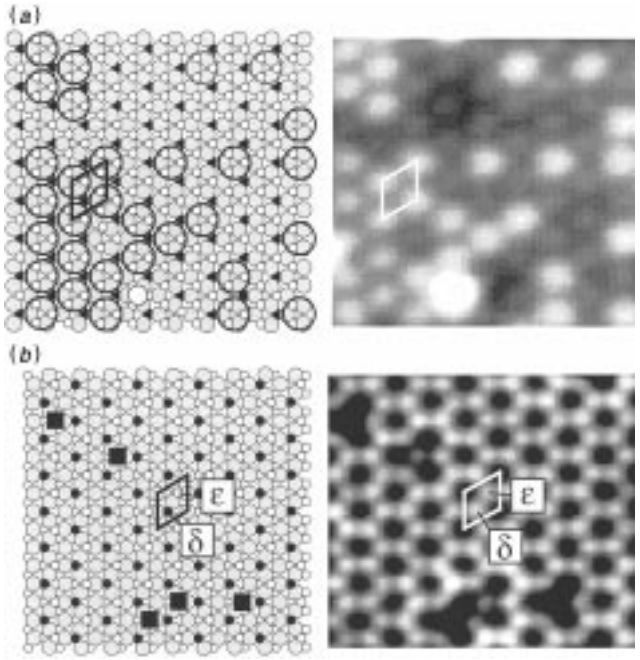

Fig. 25 STM images of $Fe_3O_4(111)$ showing the two types of image (referred to as A and B in the text) in the right hand panels of (*a*) and (*b*) respectively. Models for the terraces are shown in the left hand panels. In both cases the large grey circles are O atoms. In (*a*) the small white circles are Fe_{oct2} atoms. These group into trimer pairs each capped with an O atom represented by a large black circle. The capped trimers define the unit cell as shown in the figure. Fe atoms in the underlying layer are represented by small black circles (Fe_{tet1}) and small white circles (Fe_{oct1}). In (*b*) Fe_{oct1} atoms (labelled ε) are drawn as small white circles and Fe_{tet1} atoms (labelled δ) as small dark circles. Fe_{oct2} atoms in the underlying Fe layer are drawn as small white circles. Vacancies at Fe_{oct1} (ε) positions are designated by black squares. Reproduced with permission from ref. 42.

temperatures of around 1100 K showed a biphase hexagonal superstructure with two types of triangular mesoscopic island.[43] The hexagonal superlattice had a cell length of about 50 Å. It was shown that the islands involved co-existing $Fe_3O_4(111)$ and FeO(111) islands. The greater periodicity of this superstructure as compared with that found on $Fe_2O_3(0001)$ can be explained in terms of the better match between O—O separation in Fe_3O_4 and FeO as compared with Fe_2O_3 and FeO.

7 Dynamic studies of adsorbates on oxide surfaces

As discussed in Section 5, Onishi and coworkers have shown that formate ions adsorbed on TiO_2 surfaces can be imaged under negative sample bias as extremely bright greyscale maxima. At saturation coverage on the (1×1) reconstructed $TiO_2(110)$ surface, the formate ions form an ordered (2×1) layer. Assuming that the formate bonds to the surface Ti ions *via* oxygen ions, this saturates all the available surface Ti sites because each formate ion contains two oxygen ions. In an extremely elegant experiment,[45,46] a square void in the ordered overlayer of deuterated formate ions was created by scanning the STM tip across a 200 Å × 200 Å area of the saturated surface at +4.5 V sample bias. The mechanism for formate desorption in the proximity of the tip was not established, although a field induced mechanism was postulated. At room temperature the formate ions have significant mobility and over a timescale of the order of 60 minutes, ions are observed to diffuse into the void area (Fig. 26). The surface diffusion of formate ions was found to be highly anisotropic, with much greater mobility along the Ti rows in the [001] direction than across the O ridges that are encountered in the [110] direction.

The ability of STM to image simple molecules in a direct way clearly allows surface coverages to be determined simply by counting the number of molecules in a defined area. This idea was exploited to study the kinetics of decomposition of acetate ions on $TiO_2(110)$. At saturation coverage, acetate ions form a (2×1) overlayer on $TiO_2(110)$ (1×1) and, as with formate, the acetate ions are imaged as greyscale maxima at

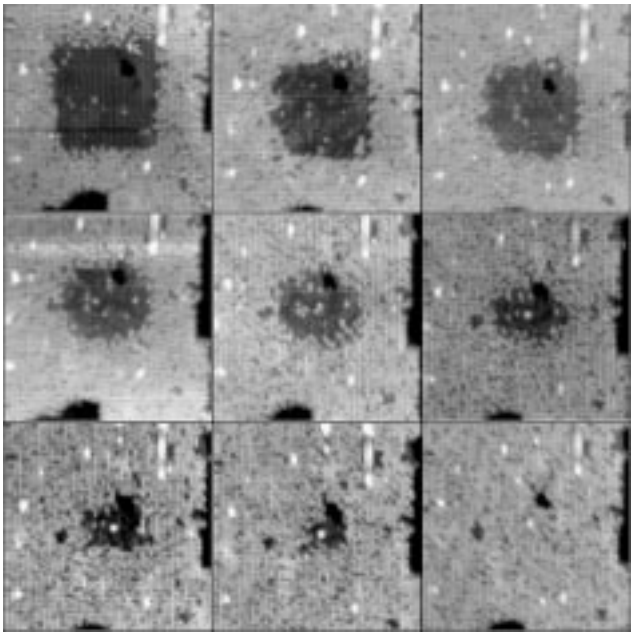

Fig. 26 Series of empty state STM images (320 Å × 320 Å, +1.0 V, 0.3 nA) of (2×1) deuteroformate (DCOO) saturated $TiO_2(110)$ following desorption of formate ions from a central square region using the STM tip. The elapse times at room temperature increase from top left to bottom right panel in the order 0.5 min, 9 min, 15 min (top row), 30 min, 40 min, 45 min (centre row) 51 min, 60 min, 79 min (bottom row). Reproduced with permission from ref. 45.

positive sample bias (Fig. 27). By subjecting a crystal surface to a temperature jump from 510 K to 540 K, it was possible to induce decomposition of the adsorbed acetate ions.[47] The number of ions appearing in a 100 Å × 100 Å scan was counted in series of frames at an interval of 16.6 s per frame. The decrease in the number of adsorbed atoms per frame followed the expected first order decay (Fig. 28). From the analysis it was possible to derive a first order rate constant of $(4 \pm 1) \times 10^{-3}$ s^{-1}.

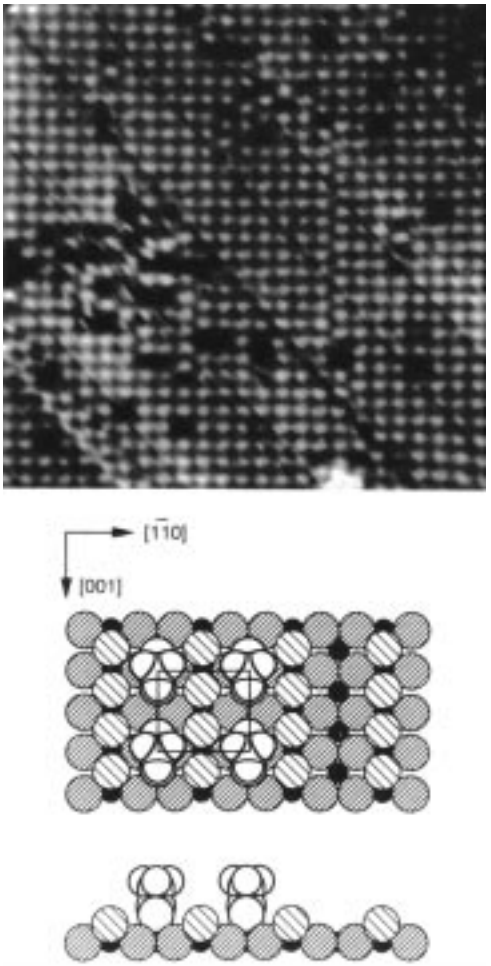

Fig. 27 Bottom panel: model for a (2 × 1) acetate monolayer on TiO_2(110). Top panel: STM image of a (2 × 1) acetate monolayer on TiO_2(110) acquired at +2.0 V sample bias and 0.3 nA tunnel current. Reproduced with permission from ref. 47.

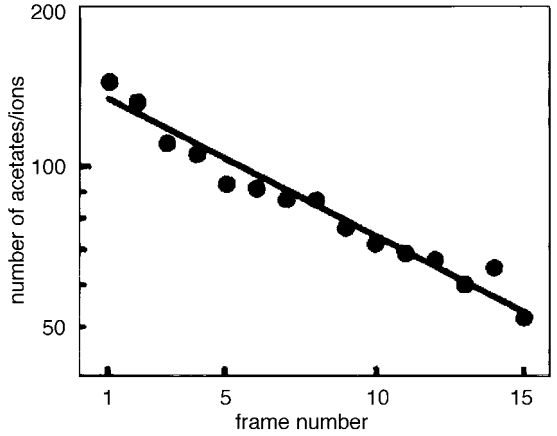

Fig. 28 Semi-log plot of number of acetate ions imaged by STM in a 100 Å × 100 Å frame on a TiO_2(110) surface that had been saturated with acetate (CH_3COO) at room temperature and then subject to a temperature jump from 510 K to 540 K against frame number. The elapse time between frames is 16.6 s. Reproduced with permission from ref. 47.

8 Concluding remarks

The application of STM to problems of oxide surface structure and dynamics has advanced very rapidly in the past few years. The technique is valuable in complementing other techniques in the study of regular periodic structures: whilst STM alone cannot provide a complete description of surface structure of the sort that could be obtained from surface X-ray diffraction or LEED it has nonetheless already proved its worth in a number of cases in establishing initial models for more refined subsequent analysis. Of perhaps greater long term importance is the ability of STM to investigate defect structures of various sorts and to characterise surfaces where one or more different terrace structures coexist on the same surface. These capabilities combined with the recent possibility to undertake STM experiments at elevated temperatures bring the technique to a point where it is now able to give a realistic atomic view of the complex sorts of surface process that are undoubtedly involved in many catalytic reactions.

References

1 V. E. Henrich and P. A. Cox, *The Surface Science of Metal Oxides*, Cambridge University Press, Cambridge, 1994.
2 H. J. Freund, H. Kuuhlenbeck and V. Staemmler, *Rep. Prog. Phys.*, 1996, **59**, 283.
3 C. J. Chen, *Introduction to Scanning Tunneling Microscopy*, Oxford University Press, Oxford, 1993.
4 R. Wiesendanger, *Scanning Probe Microscopy and Spectroscopy*, Cambridge University Press, Cambridge, 1994.
5 M. D. Kirk, J. Nogami, A. A. Baski, D. B. Mitzi, A. Kapitulnik, T. H. Geballe and C. F. Quate, *Science,* 1988, **242**, 1673.
6 C. K. Shih, R. M. Feenstra, J. R. Kirtley and G. V. Chandrashekhar, *Phys. Rev. B*, 1989, **40**, 2682.
7 M. Tanaka, S. Yamazaki, M. Fujinami, T. Takahashi, H. Katayama-Yoshida, W. Mizutani, K. Kajimura and M. Ono, *J. Vac. Sci. Technol. A*, 1990, **1**, 475.
8 X. L. Wu, C. M. Lieber, D. S. Ginley and R. J. Baughman, *Appl. Phys. Lett.*, 1989, **55**, 2129.
9 Z. Zhang and C. M. Lieber, *J. Phys. Chem.*, 1992, **96**, 2030.
10 F. H. Jones, K. Rawlings, J. S. Foord, P. A. Cox, R. G. Egdell, J. B. Pethica and B. M. R. Wanklyn, *Phys. Rev. B*, 1995, **52**, R14392.
11 F. H. Jones, K. Rawlings, J. S. Foord, P. A. Cox, R. G. Egdell, J. B. Pethica, B. M. R. Wanklyn, S. C. Parker and P. M. Oliver, *Surf. Sci.*, 1996, **359**, 107.
12 P. M. Oliver, S. C. Parker, R. G. Egdell and F. H. Jones, *J. Chem. Soc., Faraday Trans.*, 1996, **92**, 2049.
13 F. H. Jones, R. A. Dixon and A. Brown, *Surf. Sci.*, 1996, **369**, 343.
14 R. A. Dixon, J. J. Williams, D. Morris, J. Rebane, F. H. Jones and R. G. Egdell, *Surf. Sci.*, in press.
15 G. S. Rohrer, W. Lu, M. L. Norton, M. A. Blake and C. L. Rohrer, *J. Solid State Chem.*, 1994, **109**, 359.
16 F. H. Jones, K. Rawlings, S. Parker, J. S. Foord, P. A. Cox, R. G. Egdell and J. B. Pethica, *Surf. Sci.*, 1995, **336**, 181.
17 F. H. Jones, K. Rawlings, J. S. Foord, P. A. Cox and R. G. Egdell, *J. Chem. Soc., Chem. Commun.*, 1985, 2419.
18 G. S. Rohrer, V. E. Henrich and D. A. Bonnell, *Science*, 1990, **250**, 1239.
19 G. S. Rohrer, V. E. Henrich and D. A. Bonnell, *Surf. Sci.*, 1992, **278**, 146.
20 M. Sander, and T. Engel, *Surf. Sci.,* 1994, **302**, L263.
21 D. Novak, E. Garfunkel and T. Gustafsson, *Phys. Rev. B*, 1994, **50**, 5000.
22 H. Onishi and Y. Iwasawa, *Surf. Sci.,* 1994, **313**, L783.
23 H. Onishi and Y. Iwasawa, *Chem. Phys. Lett.,* 1994, **226**, 111.
24 Y. Yamaguchi, H. Onishi and Y. Iwasawa, *J. Chem. Soc., Faraday Trans.*, 1995, **91**, 1661.
25 H. Onishi, K. Fukui and Y. Iwasawa, *Bull. Chem. Soc. Jpn.*, 1995, **68**, 2447.
26 S. Fischer, A. W. Munz, K. D. Schierbaum and W. Gopel, *Surf. Sci.*, 1995, **337**, 17.
27 P. W. Murray, N. G. Condon and G. Thornton, *Phys. Rev. B*, 1995, **51**, 10989.

28 S. Fischer, A. W. Munz, K. D. Schierbaum and W. Gopel, *J. Vac. Sci. Technol. B*, 1996, **14**, 961.
29 H. Onishi and Y. Iwasawa, *Phys. Rev. Lett*., 1996, **76**, 791.
30 U. Diebold, J. F. Anderson, K. O. Ng and D. Vanderbilt, *Phys. Rev. Lett*., 1996, **77**, 1322.
31 O. Gulseren, R. James and D. W. Bullett, *Surf. Sci*., 1997, **377–379**, 150.
32 P. W. Murray, F. M Leibsle, H. J. Fisher, C. F. J. Flipse, C. A. Muryn and G. Thornton, *Phys. Rev. B*, 1992, **46**, 12877.
33 P. W. Murray, F. M. Leibsle, C. A. Muryn, H. J. Fisher, C. F. J. Flipse and G. Thornton, *Surf. Sci*., 1994, **321**, 217.
34 P. W. Murray, F. M. Leibsle, C. A. Muryn, H. J. Fisher, C. F. J. Flipse and G. Thornton, *Phys. Rev. Lett*., 1994, **72**, 689.
35 P. W. Murray, J. K. Gimzewski, R. R. Schittler and G. Thornton, *Surf. Sci*., 1996, **367**, L79.
36 P. W. Murray, J. Shen, N. G. Condon, S. J. Pang and G. Thornton, *Surf. Sci*., 1997, **380**, L455.
37 N. G. Condon, P. W. Murray, F. M. Leibsle, G. Thornton, A. R. Lennie and D. J. Vaughan, *Surf. Sci*., 1994, **310**, L609.
38 N. G. Condon, F. M. Leibsle, A. R. Lennie, P. W. Murray, D. J. Vaughan and G. Thornton, *Phys. Rev. Lett.,* 1995, **75**, 1961.
39 R. Wiesendanger, I. V. Shvets, D. Burgler, G. Tarrach, H. J. Gutherodt, J. M. D. Coey and S. Graser, *Science*, 1992, **255**, 583.
40 G. Tarrach, D. Burgler, T. Schaub, R. Wiesendanger and H. J. Guntherodt, *Surf. Sci*., 1993, **285**, 1.
41 R. Jansen, V. A. M. Brabers and H. van Kempen, *Surf. Sci*., 1995, **328**, 237.
42 A. R. Lennie, N. G. Condon, F. M. Leibsle, P. W. Murray, G. Thornton and D. J. Vaughan, *Phys. Rev. B*, 1996, **53**, 10244.
43 N. G. Condon, F. M. Leibsle, T. Parker, A. R. Lennie, D. J. Vaughan and G. Thornton, *Phys. Rev. B*, 1997, **55**, 15885.
44 F. M. Leibsle, P. W. Murray, N. G. Condon and G. Thornton, *J. Phys. D: Appl. Phys*., 1997, **30**, 741.
45 H. Onishi and Y. Isawara, *Langmuir*, 1994, **10**, 4414.
46 H. Onishi and Y. Isawara, *Surf. Sci*., 1996, **357–358**, 773.
47 H. Onishi, Y. Yamaguchi, K. Fukui and Y. Isawara, *J. Phys. Chem*., 1996, **100**, 9582.
48 F. H. Jones, R. Dixon, J. S. Foord, R. G. Egdell and J. B. Pethica, *Surf. Sci*., 1997, **376**, 367.
49 J. Buisset, H.-P. Rust, E. K. Schweizer, L. Cramer and A. M. Bradshaw, *Surf. Sci*., 1996, **349**, L147.
50 J. Tersoff and D. R. Hamann, *Phys. Rev. Lett*., 1983, **50**, 1998.
51 G. Doyen, E. Kotter, J. P. Vigneron and M. Scheffler, *Appl. Phys. A*, 1990, **51**, 281.
52 P. Sautet and C. Joachim, *Chem. Phys. Lett*., 1991, **185**, 23.
53 P. Sautet, J. C. Dunphy, D. F. Ogletree, C. Joachim and M. Salmeron, *Surf. Sci*., 1994, **315**, 127.
54 H. Galloway, P. Sautet and M. Salmeron, *Phys. Rev. B,* 1996, **54**, 11145.
55 V. P. S Awana, S. B. Samanta, P. K. Dutta, E. Gmelin and A. V. Narlikar, *J. Phys.: Condens. Matter*, 1991, **3**, 8893.
56 C. K Shih, R. M. Feenstra and G. V. Chandrashekhar, *Phys. Rev. B*, 1991, **43**, 7913.
57 Y. S. Luo, Y. N. Yang and J. H. Weaver, *Phys. Rev. B*, 1992, **46**, 1114.
58 Z. Zhang and C. M. Lieber, *Phys. Rev. B*, 1992, **46**, 5845.
59 M. Oda, C. Manabe and M. Ido, *Phys. Rev. B*, 1996, **53**, 2253.
60 Ch. Renner and O. Fischer, *Phys. Rev. B*, 1995, **51**, 9208.
61 X. L. Wu, Y. L. Wang, Z. Zhang and C.M. Lieber, *Phys. Rev. B*, 1991, **43**, 8729.
62 Z. Zhang, C.-C. Chen and C. M. Lieber, *Phys. Rev. B*, 1992, **45**, 982.
63 Z. Zhang, C. M. Lieber, D. S. Ginley, R. J. Baughman and B. Morosin, *J. Vac. Sci. Technol. B*, 1991, **9**, 1009.
64 P. K. Dutta, S. B. Samanta, A. V. Narlikar, C. Chen, J. W. Hodby and B. M. R. Wanklyn, *Philos. Mag. A*, 1992, **66**, 507.
65 L. E. C. Van de Leemput, P. J. M. Van Bentum, L. W. M. Schreurs and H. Van Kempen, *Physica C*, 1988, **152**, 99.
66 L. E. C. Van de Leemput, P. J. M. Van Bentum, H. Van Kempen and L. W. M. Schreurs, *Physica C*, 1988, **153–155**, 996.
67 H. L. Edwards, J. T. Markert and A. L. de Lozanne, *Phys. Rev. Lett*., 1992, **69**, 2967.
68 H. L. Edwards, D. J. Derro, A. L. Barr, J. T. Markert and A. L. de Lozanne, *Phys. Rev. Lett*., 1995, **75**, 1387.
69 I. Maggio-Aprile, Ch. Renner, A. Erb, E. Walker and O. Fischer, *Phys. Rev. Lett*., 1995, **75**, 2754.
70 S. Ikebe, K. Suzuki and H. Nishikawa, *Jpn. J. Appl. Phys*., 1992, **31**, 2221.
71 F. H. Jones, R. G. Egdell, A. Brown and F. R. Wondre, *Surf. Sci*., 1997, **374**, 80.
72 J. Heil, J. Wesner, B. Lommel, W. Assmus and W. Grill, *J. Appl. Phys*., 1989, **65**, 5220.
73 D. Anselmetti, R. Wiesendanger, H. J. Guntherodt and G. Gruner, *Europhys. Lett*., 1990, **12**, 241.
74 G. Rudd, D. Novak, D. Saulys, R. A. Bartynski, S. Garofalini, K. V. Ramanujachary, M. Greenblatt and E. Garfunkel, *J. Vac. Sci. Technol. B*, 1991, **9**, 909.
75 A. Zettl, L. C. Bourne, J. Clarke, M. F. Crommie, M. F. Hundley, R. E. Thompson and V. Walter, *Synth. Met*., 1989, **29**, F445.
76 U. Walter, R. E. Thomson, B. Burk, M. F. Crommie, A. Zettl and J. Clarke, *Phys. Rev. B*, 1992, **45**, 11474.
77 W. Lu, N. Nevins, M. L. Norton and G. S. Rohrer, *Surf. Sci*., 1993, **291**, 395.
78 S. C. Langford, M. Zheni, L. C. Jensen and J. T. Dickinson, *J. Vac. Sci. Technol. A*, 1990, **8**, 3470.
79 T. Matsumoto, H. Tanaka, T. Kawai and S. Kawai, *Surf. Sci*., 1992, **278**, L153.
80 Y. Liang and D. A. Bonnell, *Surf. Sci*., 1993, **285**, L510.
81 H. Tanaka, T. Matsumoto, T. Kawai and S. Kawai, *Surf. Sci*., 1994, **318**, 29.
82 Q. Jiang and J. Zegenhagen, *Surf. Sci*., 1996, **367**, L42.
83 H. Bando, T. Shimitzu, Y. Aiura, Y. Harauyama, K. Oka and Y. Nishihara, *J. Vac. Sci. Technol. B*, 1996, **14**, 1060.
84 R. L. Smith, W. Lu and G. S. Rohrer, *Surf. Sci*., 1995, **322**, 293.
85 R. L. Smith, G. S. Rohrer, K. S. Lee, D. K. Seo and M. H. Whangbo, *Surf. Sci*., 1996, **367**, 87.
86 R. A. Goschke, K. Vey, M. Maier, U. Walter, E. Goering, M. Klemm and S. Horn, *Surf. Sci*., 1996, **348**, 305.
87 M. L. Norton, J. G. Mantovani and R. J. Warmack, *J. Vac. Sci. Technol. A*, 1989, **7**, 2898.
88 G. S. Rohrer, W. Lu, R. L. Smith and A. Hutchinson, *Surf. Sci*., 1993, **292**, 261.
89 R. L. Smith and G. S. Rohrer, *J. Solid State Chem*., 1996, 124, 104.
90 M. R. Castell, P. L. Wincott, N. G. Condon, C. Muggelberg, G. Thornton, S. L. Dudarev, A. P. Sutton and G. A. D. Briggs, *Phys. Rev. B*, 1997, **55**, 7859.
91 M. R. Castell, C. Muggelberg, G. A. D. Briggs and D. T. Goddard, *J. Vac. Sci. Technol. B*, 1996, **14**, 966.
92 C. Muggelberg, M. R. Castell, G. A. D. Briggs and D. T. Goddard, *Proc. 4th Nordic Conf. Surf. Sci*, ed. S. Raaen and J. Bremer, 1997, p. 103.
93 M. Baumer, D. Cappus, H. Kuhlenbeck, H. J. Freund, G. Wilhelmi, A. Brodde and H. Neddermeyer, *Surf. Sci*., 1991, **253**, 116.
94 F. Rohr, M. Baumer, H. J. Freund, J. A. Meijas, V. Staemmler, S. Muller, L. Hammer and K. Heinz, *Surf. Sci*., 1997, **372**, L291.
95 N. M. D. Brown and H. You, *Surf. Sci*., 1990, **233**, 317.
96 C. A. Ventrice, H. Hannemann, A. Brodde and H. Neddermeyer, *Phys. Rev. B*, 1994, **49**, 5773.
97 H. C. Galloway, J. J. Benitez and M. Salmeron, *J. Vac. Sci. Technol. A,* 1994, **12**, 2302.
98 C. Xu and D. W. Goodman, *Chem. Phys. Lett*., 1996, **263**, 13.
99 Th. Bertrams, F. Winkelman, Th. Uttich, H. J. Freund and H. Neddermeyer, *Surf. Sci*., 1995, **331–333**, 1515.
100 J. Libuda, F. Winkelman, M. Baumer, H. J. Freund, Th. Bertrams, H. Neddermeyer and K. Muller, *Surf. Sci*., 1994, **318**, 61.
101 M. Baumer, J. Libuda, A. Sandell, H. J. Freund, G. Graw, Th. Bertrams and H. Neddermeyer, *Ber. Bunsen-Ges. Phys. Chem*., 1995, **99**, 1381.
102 S. Stemple, M. Baumer, M. Frank, J. Libuda and H. J. Freund, *Proc. 4th Nordic Conf. Surf. Sci*., ed. S. Raaen and J. Bremer, 1997, p. 112.
103 J. B. Pethica, *Phys. Rev. Lett*., 1986, **57**, 3235.
104 M. Kielwein, K. Saiki, G. Roth, J. Fink, G. Paasch and R. G. Egdell, *Phys. Rev. B*, 1995, **51**, 10320.
105 D. W. Bullett, *J. Phys. C*, 1983, **16**, 2197.
106 M. C. Wu and P. J. Moller, *Surf. Sci*., 1989, **224**, 265.
107 Q. Guo, I. Cocks and E. M. Williams, *Phys. Rev. Lett*., 1996, **77**, 3851.

Paper 7/06191I; *Received* 26*th August*, 1997